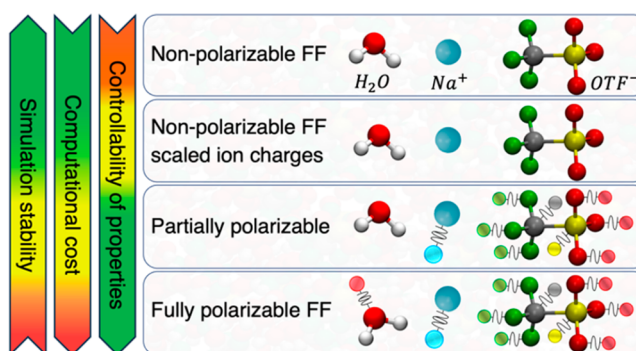


Molecular Modeling of Water-in-Salt Electrolytes: A Comprehensive Analysis of Polarization Effects and Force Field Parameters in Molecular Dynamics Simulations

Majid Rezaei,* Sung Sakong, and Axel Groß

ABSTRACT: Accurate modeling of highly concentrated aqueous solutions, such as water-in-salt (WiS) electrolytes in battery applications, requires proper consideration of polarization contributions to atomic interactions. Within the force field molecular dynamics (MD) simulations, the atomic polarization can be accounted for at various levels. Nonpolarizable force fields implicitly account for polarization effects by incorporating them into their van der Waals interaction parameters. They can additionally mimic electron polarization within a mean-field approximation through ionic charge scaling. Alternatively, explicit polarization description methods, such as the Drude oscillator model, can be selectively applied to either a subset of polarizable atoms or all polarizable atoms to enhance simulation accuracy. The

trade-off between simulation accuracy and computational efficiency highlights the importance of determining an optimal level of accounting for atomic polarization. In this study, we analyze different approaches to include polarization effects in MD simulations of WiS electrolytes, with an example of a Na-OTF solution. These approaches range from a nonpolarizable to a fully polarizable force field. After careful examination of computational costs, simulation stability, and feasibility of controlling the electrolyte properties, we identify an efficient combination of force fields: the Drude polarizable force field for salt ions and non-polarizable models for water. This cost-effective combination is sufficiently flexible to reproduce a broad range of electrolyte properties, while ensuring simulation stability over a relatively wide range of force field parameters. Furthermore, we conduct a thorough evaluation of the influence of various force field parameters on both the simulation results and technical requirements, with the aim of establishing a general framework for force field optimization and facilitating parametrization of similar systems.



1. INTRODUCTION

Electrochemical energy storage using secondary batteries is a critical component for our future sustainable energy economy. Currently, Li-ion batteries (LiBs) are dominating the market for high-performance batteries. Since their commercialization over thirty years ago, the performance of LiBs has constantly improved.¹ However, in spite of technological progress that is still possible, the LiB technology is facing physicochemical limits of its performance.² Furthermore, there are concerns with regard to safety aspects³ and with the sustainability of the materials used in LiBs.⁴ As one of the main causes for hazards in battery operation, dendrite growth at the anodes has been identified.⁵ This can lead to short-circuits, which together with flammable electrolytes might result in battery fires. One option to reduce these fire risks is to use non-flammable electrolytes such as ionic liquids.^{6,7} However, the high costs of such ionic liquids still prevent their commercialization. Aqueous electrolytes would be ideal^{8,9} as they combine nonflammability with excellent transport properties. However, they are limited by their small potential window of electrochemical stability. As a

promising alternative, water-in-salt (WiS) electrolytes have recently been introduced.^{10,11} They are based on the concept of using dissolved salts in extremely high concentrations, higher than the concentration of water molecules. As a consequence, all water molecules are involved in building up the solvation shell of the charge carrier, so that hardly any free water molecules are present. Thus, there are no longer any weak hydrogen bonds between water molecules present, but only stronger water-ion bonds. This can increase the electrochemical stability window to values above 3 V.¹² This water-in-salt concept has first been applied to LiBs, but it has also been extended to sodium-ion batteries [NaBs].¹³ Sodium is much more earth-abundant than lithium, and production of

NaBs typically does not require any critical raw materials. Recently, NaBs have drawn a lot of attention as an alternative cell chemistry for both mobile and stationary applications.^{14,15} Although their energy densities and cyclability can still not fully compete with LiBs, NaBs promise to be less expensive and have better charging and ion mobility properties.

Still, there is a need to better understand the properties of sodium-ion batteries with WiS electrolytes. From a theoretical point of view, this requires performing molecular dynamics (MD) simulations in order to take the liquid nature of the WiS electrolytes appropriately into account. Ab initio molecular dynamics (AIMD) simulations¹⁶ would be the ideal choice as they combine a proper description of the chemical interactions with statistical sampling. However, due to their high computational effort, typically only small system sizes and short simulation times can be considered. In contrast, classical force fields allow MD simulations to be run for sufficiently large system sizes and long simulation times, but they suffer from a limited accuracy as far as the chemical interactions are concerned. So far, good efforts have been made to model WiS solutions using classical MD simulations^{17–22} for LiB electrolytes. However, there are only a few studies on NaB electrolytes. Furthermore, there are still concerns about the accuracy of the force fields used for the simulation of WiS solutions, particularly with regard to how they account for polarization effects, which are of paramount importance at high salt concentrations. There are attempts to model Na⁺ ions in different WiS solutions^{23–25} using the nonpolarizable force fields OPLS²⁶ and GAFF.²⁷ Kartha and Mallik,²⁸ however, reported that nonpolarizable force fields are insufficient to accurately reproduce the transport properties of such solutions. They demonstrated that ionic charge scaling can improve the dynamic properties of NaTFSI and LiTFSI WiS electrolytes. The ionic charge scaling method has also been widely used in ionic liquid simulations.^{29–33} To enhance the accuracy of both the dynamic and structural properties of Na-WiS electrolytes, Jiang et al.³⁴ employed the quantum-chemistry-based polarizable force field APPLE&P.³⁵ This proprietary model is promising, but its force field parameters are not available in the open literature, and its uncommon functional form presents a challenge in extending its application to different compounds or materials.³⁶ More general polarizable force fields, such as Drude-based models,³⁷ can be easily applicable for a broader range of systems, including various types of ionic liquids.^{36,38,39} Notably, the Drude-based SAPT-FF model⁴⁰ has been employed to model ionic liquids⁴¹ and their mixtures with different solvents,^{42,43} including water (the SWM4-NDP water model⁴⁴), at a wide range of concentrations. However, the available parameters from the literature for the Drude polarizable force fields are limited to predict the properties of the electrolytes like ionic liquids in Na-ion batteries accurately,⁴⁵ highlighting the importance of further improvement.

In the present work, as a first step to reliably assess the properties of WiS electrolytes in NaBs, we have tested and compared four different force fields. Our particular focus is on their description of atomic polarization, which is crucial for WiS electrolyte modeling. We will discuss the performance of the force fields in terms of computational effort, simulation stability, and controllability of the electrolyte properties to identify an optimal level of accounting for atomic polarization. At the same time, we will identify the chemical and physical properties of the electrolyte that are crucial for its use in NaBs.

Finally, the dependence of the electrolyte properties on force field parameters will be examined to establish a general framework for force field parametrization.

2. NUMERICAL METHODS

2.1. Force Field Construction. We aim to model a NaOTF water-in-salt (WiS) electrolyte using classical molecular dynamics simulations. For this purpose, a well-suited force field potential is essential to evaluate the electrolyte properties correctly. In classical MD, the potential energy is modeled through bonded and nonbonded terms that, respectively, describe the interactions between the atoms that are linked by covalent bonds and the noncovalent interactions between all pairs of atoms:

$$U_{\text{tot}} = U_{\text{bonded}} + U_{\text{nonbonded}} \quad (1)$$

Depending on the characteristics of the system and the details to be modeled by the force field, U_{bonded} and $U_{\text{nonbonded}}$ may consist of different terms. For systems containing strongly polarizable atoms, such as WiS electrolytes, the potential energy must reflect the contribution of strong polarization. This contribution can be accounted for either implicitly or explicitly. The functional forms and the parameters of the resulting force fields are detailed in the following.

2.1.1. Nonpolarizable Force Field. We start with an all-atom force field where the polarization effect is only implicitly included in the van der Waals (VdW) and electrostatic interactions, respectively approximated with pairwise Lennard-Jones (LJ) and Coulomb potentials. The LJ term represents a combination of the short-distance interatomic repulsion and both the dispersion and polarization contributions to the VdW attractive interaction. The Coulomb term describes the long-range electrostatic interaction. By scaling the ionic charges, the electronic polarization can also be included in the Coulomb term in a mean field approximation.^{31,46,47} The nonbonded term of the potential energy is given by

$$U_{\text{nonbonded}} = w^{ij} \sum_i \sum_{j>i} \left(4\epsilon^{ij} \left[\left(\frac{\sigma^{ij}}{r^{ij}} \right)^{12} - \left(\frac{\sigma^{ij}}{r^{ij}} \right)^6 \right] + \frac{k_q^i k_q^j}{4\pi\epsilon_0 r^{ij}} \right) \quad (2)$$

where i and j run over all the atoms in the system, r^{ij} is the distance between the atoms i and j , σ^{ij} and ϵ^{ij} are the Lennard-Jones size and interaction strength, respectively, ϵ_0 is the vacuum permittivity, q^{ij} is the atomic (partial) charge, k_q^{ij} is a factor that uniformly scales down ionic charges to approximate electronic polarization (see eq 3), and w^{ij} is a weighting coefficient for pairwise intramolecular interaction energy (given by eq 4).

$$k_q^i = \begin{cases} K_q \leq 1 & \text{if } i \in \text{ions} \\ 1 & \text{otherwise} \end{cases} \quad (3)$$

$$w_{ij} = \begin{cases} 0 & \text{if } ij \in b_1 \\ 0 & \text{if } ij \in b_2 \\ 0.5 & \text{if } ij \in b_3 \\ 1 & \text{otherwise} \end{cases} \quad (4)$$

b_1 , b_2 , and b_3 in eq 4 are the sets of atom pairs that are connected by direct bonds, via one intermediate bond, and via two intermediate bonds, respectively. The LJ parameters σ^{ij}

and ε^{ij} in eq 2 are calculated using geometric means of the parameters for atoms i and j , $\sigma^{ij} = \sqrt{\sigma^i \sigma^j}$, and $\varepsilon^{ij} = \sqrt{\varepsilon^i \varepsilon^j}$.

Whereas the interactions of the monatomic cations (Na^+) can be fully represented by the nonbonded terms described in eq 2, water and anion (OTF^-) molecules require additional terms to describe their molecular configurations and intramolecular covalent interactions. Considering the two-body, three-body angular, and four-body dihedral intramolecular interactions, the bonded potential energy is written as

$$U_{\text{bonded}} = \sum_{ij \in \text{bonds}} k_b^{ij} (r^{ij} - r_0^{ij})^2 + \sum_{ijk \in \text{angles}} k_\theta^{ijk} (\theta^{ijk} - \theta_0^{ijk})^2 + \sum_{ijks \in \text{dihedrals}} \sum_{m=1}^4 \frac{k_m^{ijks}}{2} [1 + (-1)^{m+1} \cos(m\phi_0^{ijks})] \quad (5)$$

where are the atom groups for the corresponding intramolecular interactions; k_b^{ij} , k_θ^{ijk} , and k_m^{ijks} are the force constants; r_0^{ij} is the optimal bond length; θ_0^{ijk} is the valence angle; and ϕ_0^{ijks} is the valence dihedral angle.

The nonpolarizable force field requires low computational costs for describing polarization effects, but the method may be unsuitable to model strongly polarized systems such as ionic liquids and WiS electrolytes. Specifically, nonpolarizable simulations of ionic liquids have been shown³⁹ to miss crucial physics and interactions, which can only be captured by explicitly describing atomic polarization.

2.1.2. Drude Polarizable Force Field. The Drude oscillator model^{37,48} (also referred to as the core-shell or charge-on-spring model^{49,50}) explicitly accounts for the dynamics of the electric dipole moments on polarizable atoms. In this model, the polarizable atom consists of a pair of charged particles, i.e., a negatively charged Drude particle (DP or shell⁵¹) and a positively charged Drude core (DC). Since the DC carries the majority of the atomic mass, the DP models a fluctuating electron cloud around the core atom. These two particles are bound by a harmonic potential

$$U_D = \frac{k_D}{2} r_D^2 \quad (6)$$

with k_D being the spring constant and r_D being the DP-DC distance. The partial charges $q' + q_D$ and $-q_D$ are, respectively, assigned to DC and DP, where q' is the atomic partial charge in the corresponding nonpolarizable force field (see eq 2) and q_D is the point charge representing the induced dipole on the polarizable atom. q_D and k_D are related through

$$\alpha = \frac{q_D^2}{k_D} \quad (7)$$

with α being the atomic polarizability, which is generally the sum of two contributions: the distortion of the electron cloud around the nucleus and the interatomic charge redistribution caused by the local electric field. Drude oscillators mainly model the first contribution. The second contribution can be

accounted for using fluctuating partial charges,⁵² which is beyond the subject of this paper. To avoid overestimation of polarization effects when using experimentally or computationally measured overall polarizabilities in the Drude model, suitable control factors⁴⁸ or appropriate damping of dipolar interactions can be introduced, as will be discussed later. In this study, k_D takes a standard value from the literature (see section 2.2.2), and q_D is calculated for individual atom types from eq 7. We employ a scalar k_D for all Drude oscillators, which makes their response to local electric fields independent of the field direction. Nevertheless, the intramolecular electrostatic interactions between oscillators lead to an anisotropic molecular polarizability, as it occurs in polar molecules. To describe the local anisotropy around lone pairs more precisely, one must expand k_D into a tensor form by setting off-diagonal elements to zero, which describes the orientation-dependent deformation of Drude oscillators (see refs 48, 53, and 54).

The DPs interact purely electrostatically, but nonbonded interactions of other particles (DCs and nonpolarizable atoms) include both LJ and Coulomb contributions (see eq 2). For the LJ interactions, one can use the same parameters as in nonpolarizable counterparts. However, since the LJ potential in nonpolarizable force fields already includes the polarization contribution to the VdW interaction implicitly, the LJ interactions of DCs must be rescaled to avoid double counting of the polarization effect. In practice, we use the fragment-base scaling factor proposed by Goloviznia et al.^{36,55}

$$k_{LJ}^{ij} = \left(1 + 0.25 \bar{r}_0^{ij2} \frac{\bar{q}^i \bar{\alpha}^j + \bar{q}^j \bar{\alpha}^i}{\bar{\alpha}^i \bar{\alpha}^j} + 0.11 \frac{\bar{\mu}^i \bar{\alpha}^j + \bar{\mu}^j \bar{\alpha}^i}{\bar{\alpha}^i \bar{\alpha}^j} \right)^{-1} \quad (8)$$

where i and j denote a pair of DCs belonging to two different polarizable fragments; \bar{q}^i , $\bar{\alpha}^i$, and $\bar{\mu}^i$ are, respectively, the net charge, molecular polarizability, and dipole moment of the fragment containing atom i ; and \bar{r}_0^{ij} is the equilibrium distance between the centers of mass of the fragments containing atoms i and j . We set $\bar{r}_0^{ij} = 4.17 \text{ \AA}$ for the interactions between Na^+ and OTF^- , which is obtained from ab initio molecular dynamics calculations done in a similar fashion as described in refs 16 and 56. As will be shown later in eq 13, k_{LJ}^{ij} is applied to the LJ term of the nonbonded DC-DC interactions.

The scaling factor given by eq 8 is applicable when combining the Drude model with a nonpolarizable water force field. When using an explicitly polarizable water model, such as the SWM4-NDP (see section B in the Supporting Information), k_{LJ}^{ij} should be selectively applied to LJ interactions. In this case, the scaling factor described in eq 8 can be fully applied to ion-ion LJ interactions. For water-ion interactions, however, it should be modified to only account for the influence of water molecules on ions.³⁶ Accordingly, eq 8 can be detailed for each pair interaction as

$$k_{LJ}^{ij} = \begin{cases} 1 & \text{if } i \text{ and } j \in \text{DC}_w \\ \left(1 + 0.25\bar{r}^{ij2} \frac{\bar{q}^i \bar{\alpha}^j + \bar{q}^j \bar{\alpha}^i}{\bar{\alpha}^i \bar{\alpha}^j} + 0.11 \frac{\bar{\mu}^i \bar{\alpha}^j + \bar{\mu}^j \bar{\alpha}^i}{\bar{\alpha}^i \bar{\alpha}^j} \right)^{-1} & \text{if } i \text{ and } j \notin \text{DC}_w \\ \left(1 + 0.25\bar{r}^{ij2} \frac{\bar{q}^{w2}}{\bar{\alpha}^w} + 0.11 \frac{\bar{\mu}^{w2}}{\bar{\alpha}^w} \right)^{-1} \simeq 0.72 & \text{otherwise} \end{cases} \quad (9)$$

where DC_w is the set of DCs for already polarizable water molecules. By considering the dipole moment, molecular polarizability, and net charge of water molecules, $\bar{\mu}^w = 1.855$ D,⁵⁷ $\bar{\alpha}^w = 0.97825$ Å³,⁴⁴ and $\bar{q}^w = 0$, eq 9 gives the scaling factor for ion–water interaction as $k_{LJ}^{ij} \simeq 0.72$. In the present study, we coin the force fields that combine the Drude oscillator model with nonpolarizable and polarizable water models as “partially” and “fully” polarizable force fields, respectively.

When a Drude oscillator model is applied, there is a technical difficulty in maintaining the simulation stability for a long MD trajectory. Specifically, the strong dipole–dipole interactions at a short distance can cause an overestimated correlation between dipoles, which is known as “polarization catastrophe”.⁵⁸ To control the short-distance electrostatic interactions, we employ the Thole damping function⁵⁹

$$T^{ij}(r^{ij}) = 1 - \left(1 + \frac{s^{ij} r^{ij}}{2} \right) \exp(-s^{ij} r^{ij}) \quad (10)$$

where the scaling parameter s^{ij} is determined by the atomic polarizabilities α^{ij} and a damping parameter a^{ij}

$$s^{ij} = \frac{a^i + a^j}{2(\alpha^i \alpha^j)^{1/6}} \quad (11)$$

The Thole damping function is applied to the interactions between the point charges representing the induced dipoles on polarizable atoms, i.e., the charges on DPs, $-q_D^i$, and the opposite charges located on the respective DCs, q_D^j (the latter is only part of the full charges of DCs).

In the presence of small highly charged atoms, such as Na^+ , Thole damping alone is not sufficient to avoid instabilities,³⁶ and additional damping is required. For this purpose, we use a modified Tang–Toennies (TT) function,⁶⁰ as proposed by Goloviznina et al.⁶¹

$$f_{\text{TT}}^{ij}(r^{ij}) = \begin{cases} 1 - c_{\text{TT}} e^{-b_{\text{TT}} r^{ij}} \sum_{k=0}^4 \frac{(b_{\text{TT}} r^{ij})^k}{k!} & i \text{ or } j \in \text{DC}_{\text{Na}} \\ 1 & \text{otherwise} \end{cases} \quad (12)$$

where b_{TT} and c_{TT} adjust the interaction strength and DC_{Na} denotes the group of DCs of Na^+ ions. The TT damping function is applied to the interactions between the nonpolarizable part of the charges on the DCs of Na^+ ions, $q^i = q^i - q_D^i$, and the Drude charges on the DPs and DCs of the other polarizable atoms, $\pm q_D^j$ (see eq 13).

By including the modified interactions for DPs and DCs, the nonbonded term of the potential energy of a Drude polarizable force field can be written as

$$U_{\text{nonbonded}} = \sum_a \sum_{b>a} w^{ab} \left(4\epsilon^{ab} \left[\left(\frac{\sigma^{ab}}{r^{ab}} \right)^{12} - \left(\frac{\sigma^{ab}}{r^{ab}} \right)^6 \right] + \frac{q^a q^b}{4\pi\epsilon_0 r^{ab}} \right) + \sum_k \sum_{s>k} w^{ks} \left(4k_{LJ}^{ks} \epsilon^{ks} \left[\left(\frac{\sigma^{ks}}{r^{ks}} \right)^{12} - \left(\frac{\sigma^{ks}}{r^{ks}} \right)^6 \right] + \frac{(q^k - q_D^k)(q^s - q_D^s) + f_{\text{TT}}^{ks}(r^{ks})((q^k - q_D^k)q_D^s + q_D^k(q^s - q_D^s)) + T^{ks}(r^{ks})q_D^k q_D^s}{4\pi\epsilon_0 r^{ks}} \right) + \sum_m \sum_{n>m} w^{mn} \left(\frac{T^{mn}(r^{mn})q^m q^n}{4\pi\epsilon_0 r^{mn}} \right) + \sum_a \sum_k w^{ak} \left(4\epsilon^{ak} \left[\left(\frac{\sigma^{ak}}{r^{ak}} \right)^{12} - \left(\frac{\sigma^{ak}}{r^{ak}} \right)^6 \right] + \frac{q^a q^k}{4\pi\epsilon_0 r^{ak}} \right) + \sum_a \sum_m w^{am} \left(\frac{q^a q^m}{4\pi\epsilon_0 r^{am}} \right) + \sum_k \sum_m w^{km} \left(\frac{f_{\text{TT}}^{km}(r^{km})(q^k - q_D^k)q^m + T^{km}(r^{km})q_D^k q^m}{4\pi\epsilon_0 r^{km}} \right) \quad (13)$$

where the indices a and b run over nonpolarizable atoms (here, water oxygen and hydrogen), k and s run over DCs, and m and n run over DPs. The bonded term of the potential energy,

including the harmonic interactions between DPs and their respective DCs (see eq 6), is given by

$$\begin{aligned}
U_{\text{bonded}} = & \sum_{ij \in \text{bonds}} k_b^{ij} (r^{ij} - r_0^{ij})^2 + \sum_{ijk \in \text{angles}} k_\theta^{ijk} (\theta^{ijk} - \theta_0^{ijk})^2 \\
& + \sum_{ijks \in \text{dihedrals}} \sum_{m=1}^4 \frac{k_m^{ijks}}{2} [1 + (-1)^{m+1} \cos(m\varphi_0^{ijks})] \\
& + \sum_{n \in \text{dipoles}} \frac{k_D^n}{2} r_D^{n2}
\end{aligned} \tag{14}$$

with dipoles being the group of DC–DP pairs on polarizable sites.

2.2. Parameterization of the Force Field Potential. In addition to the functional form of the potential, a force field requires a set of parameters that determine the physical and chemical properties. General force field parameters describe the types of atoms, chemical bonds, molecular geometries, and nonbonded interactions. Depending on the employed methods, force fields may also require several specific parameters, such as the Drude parameters that describe dipolar interactions in the Drude polarizable force field. Parametrizing the force field is a crucial step in representing the target system properly. This requires an understanding of the relationship between the system properties and force field parameters. To achieve this, we start with a base set of force field parameters and vary the parameter values to monitor their influence on the electrolyte properties.

2.2.1. General Force Field Parameters. We have selected several water models to probe the influence of water parameters on the electrolyte properties. We start from the nonpolarizable models SPC, SPC/E, TIP3P, OPC3, SPC/Fw, and TIP4P. [Table S1](#) shows the parameters of these models. In our base nonpolarizable (BNP) and base partially polarizable (BPP) force fields, we use the SPC/E water model. We also construct a fully polarizable (FP) force field using the SWM4-NDP water model, which explicitly accounts for water polarization via Drude particles attached to water oxygens (see [Figure S2](#)). This model provides a dielectric constant close to the experimental data, which makes it suitable for where water-mediated electrostatic interactions are important.^{62,63} The parameters of this model are listed in [Table S2](#).

The interactions of Na⁺ ions are described by the LJ parameters in [eq 2](#). For this purpose, we select seven sets of ϵ^{Na} and σ^{Na} from the literature (listed in [Table S3](#)). The GROMOS⁶⁴ parameters, $\epsilon^{\text{Na}} = 0.0148$ kcal/mol and $\sigma^{\text{Na}} = 2.58$ Å, are used in the BNP, BPP, and FP force fields. For the polyatomic ion OTF⁻, in addition to the LJ parameters, the partial charges and the parameters for the bonded potentials in [eq 5](#) are also necessary. In this work, we take the force field parameters for OTF⁻ from refs [65](#) and [66](#) (see [Table S4](#)). We also apply a scaling factor, k_q , to ionic charges to include electronic polarization in our nonpolarizable simulations (see [eqs 2](#) and [3](#)). Although a charge scaling factor of 0.7–0.8 is known to reproduce reasonable thermodynamic properties for ionic liquids,⁴⁷ the optimal scaling factor is still in debate.³¹ We vary k_q from 1 to 0.7 to address the effect of charge scaling on the electrolyte properties. In the BNP force field, we set $k_q = 1$.

2.2.2. Drude Parameters. To keep DPs spatially close to their DC, we select a small Drude mass of $m_D = 0.4$ g/mol, as suggested by Lamoureux and Roux,⁶⁷ and a stiff harmonic bond of $k_D = 2000$ kcal/mol Å². A smaller m_D requires a smaller time step and may cause simulation instability. k_D in [eq 6](#) adjusts the charge of the DP (see [eq 7](#)) and its displacement

from the DC. Lamoureux and Roux⁶⁷ suggested using $k_D = 1000$ kcal/mol Å² for all types of DP–DC bonds. Heid et al.,⁶⁸ however, reported that $k_D = 2000$ kcal/mol Å² performs slightly better, as it leads to higher Drude charges and closer displacements of DPs to their cores. In this work, we vary k_D from 1000 to 4000 kcal/mol Å² to investigate its effect on the electrolyte properties. We note that for smaller values of k_D , the simulation becomes unstable.

Atomic polarizabilities are crucial, as they determine the partial charges on Drude pairs ([eq 7](#)), and impact the scaling factor for LJ interactions, k_{LJ}^{ij} ([eq 8](#)), and the Thole scaling parameter, S^{ij} ([eq 11](#)). The measured and calculated values of the atomic polarizability can be various depending on the experimental and computational methods. We set the polarizability of Na⁺ to $\alpha^{\text{Na}} = 0.157$ Å³, which was originally calculated in the gaseous phase⁶⁹, but is widely used for simulations of liquid solutions via Drude oscillators.^{70–73} A range of α^{Na} , including five values reported in the literature (see [Table S5](#)), are also tested. The polarizabilities of the OTF⁻ atoms are set according to ref [66](#) (see [Table S4](#)) and uniformly scaled by $k_\alpha^{\text{OTF}} = 0.25$ –1. It is worth noting that, since the polarizability response to a small temperature variation is negligible, we use the polarizabilities measured at 25 °C.

The parameter a^I in [eq 11](#), which adjusts the strength of the short-distance dipolar interactions, usually takes a default value of 2.6⁷⁴ (or 2.08 in the AMBER force field⁵⁸) for all polarizable atoms. In certain force fields, the value may depend on the atom types.⁴⁸ In this study, we use $a = 2.6$ for all polarizable particles. We also vary the value of this parameter to examine its effect on the electrolyte properties. Finally, in [eq 12](#), we set the same damping parameters as those suggested by Goloviznina et al.⁶¹ for certain ionic liquids, $b_{\text{TT}} = 4.5$ and $c_{\text{TT}} = 1$, the latter of which satisfies an asymptotic behavior $f_{\text{TT}}^{ij}(r^{ij}) \rightarrow 0$ when $r^{ij} \rightarrow 0$. These parameters are also tested at intervals where the simulation remains stable.

2.2.3. Base Sets of Force Field Parameters. The parameters used in our base nonpolarizable, base partially polarizable, and fully polarizable simulations (BNP, BPP, and FP force fields) are summarized in [Table 1](#).

Table 1. Parameters of Base Nonpolarizable, Base Partially Polarizable, and Fully Polarizable Force Fields

general force field parameters (for BNP, BPP, and FP simulations)	
water model	SPC/E (see Table S1) for the BNP and BPP force fields SWM4-NDP (see Table S2) for the FP force field
Na ⁺ LJ parameters	GROMOS (see Table S3)
OTF ⁻ parameters	according to ref 65 (see Table S4)
ionic charge scaling factor, K_q	1
parameters that adjust Drude interactions (only for the BPP and FP force fields)	
mass of the DPs, m_D	0.4 g/mol
DP–DC force constant, k_D	2000 kcal/mol Å ²
polarizability of Na ⁺ ions, α^{Na}	0.157 Å ³
polarizability of the atoms of OTF ⁻ anions	according to ref 66 (see Table S4)
Thole damping parameter a (see eq 11)	2.6
TT damping parameter b_{TT} (see eq 12)	4.5
TT damping parameter c_{TT} (see eq 12)	1

2.3. Simulation Setup. We use a cubic simulation box with an initial side length of 28 Å, chosen large enough that the size effect is negligible (see the SI section A), and periodic boundary conditions in all three directions. 80 salt ion pairs and 480 water molecules are randomly distributed within the simulation box, resulting in a salt concentration of 9.25 m. In the case of a NaOTF aqueous electrolyte, this salt concentration corresponds to the water-in-salt regime.^{12,75} The energy of the system is minimized via the Polak–Ribiere version of the conjugate gradient (CG) method.⁷⁶ For polarizable simulations, Drude particles are added to an energy minimized configuration using the polarizer tool described in ref 77. The initial velocity of atoms is determined using a Gaussian distribution based on the specified temperature. For the long-range Coulomb interactions, the P3M algorithm⁷⁸ is used and tuned to obtain a maximum relative error of 10^{-4} in the calculated forces. For the LJ interactions, we used a cutoff radius of 1.2 nm. All simulations are performed in LAMMPS⁷⁹ using the velocity Verlet method.

We statistically sample canonical NVT ensembles at 333 K using the Nose–Hoover thermostat with a relaxation time of 0.1 ps. For polarizable simulations, special treatment is required concerning the thermostat to keep the temperature of DPs low and ensure that Drude oscillations do not influence the kinetic energy of the atoms.⁶⁸ For this purpose, a dual Nose-Hoover thermostat is used to maintain the Drude degrees of freedom at 1 K. In the fully polarizable force field, i.e., when using the SWM4-NDP water model, the rigid water molecules are also integrated separately using an independent Nose-Hoover thermostat or barostat with chains,⁸⁰ which is applied to both the translational and rotational degrees of freedom of water molecules (see ref 81). In this case, the atomic masses, positions, velocities, and forces are converted into a reduced representation where the DCs transform into the centers of mass of the DC-DP pairs and the DPs transform into their relative positions with respect to their cores (see ref 67).

All polarizable and nonpolarizable simulations are performed in two steps. First, the pressure and volume of the system are equilibrated using a 2 ns simulation in an NPT ensemble utilizing a Nose-Hoover barostat with a target pressure of 1 atm and one or more Nose-Hoover thermostats (as described above) with a target temperature of 333 K. Subsequently, simulations are continued for 22 ns in the corresponding NVT ensemble, the last few nanoseconds of which are used to calculate the electrolyte properties, as described in section 2.4. For nonpolarizable simulations, the time step is set to 2 fs. The time step for polarizable simulations is set to 0.1–0.5 fs to make the simulations stable (the simulation stability is discussed in detail in section 3.5). All simulations are carried out on 24–48 CPU cores.

2.4. Sampling and Analysis Methods of Electrolyte Properties. *2.4.1. Dynamic Properties.* The random Brownian motion of particles diffusing in a liquid is well described by the Einstein relation:

$$\langle |r(t) - r(0)|^2 \rangle = 6Dt \quad (15)$$

where $\langle |r(t) - r(0)|^2 \rangle$ is the mean squared displacement (MSD), D is the diffusion coefficient, and t is time. According to eq 15, for sufficient statistical sampling, the slope of the linear fit to MSD versus time converges to $6D$. This requires a large enough sampling time and a sufficient number of diffusing particles. But most MD simulation methods have

computational limitations on the number of particles and simulation time, which can introduce noise and fluctuations in this curve. The resulting fluctuations can be efficiently reduced by averaging the $\text{MSD}(t)$ obtained from either different trajectories or different segments of a long enough trajectory. In this study, the last 20 ns of the trajectories are broken into 10 segments of equal length, and $\text{MSD}(t)$ is averaged over all segments (see the SI section C).

The electrolyte viscosity is extracted from the off-diagonal components of the Green–Kubo expression

$$\eta = \frac{V}{10k_{\text{B}}T} \int_0^\infty \left\langle \sum_{\alpha\beta} P_{\alpha\beta}(\tau + \tau_0) P_{\alpha\beta}(\tau_0) \right\rangle_{\tau_0} d\tau \quad (16)$$

with V being the volume of the simulation box and $P_{\alpha\beta}(\tau)$ being the stress in the $\alpha\beta$ plane as a function of time. We use the last 2.5–5 ns of the production run to calculate η from eq 16 (see SI section C).

2.4.2. Structural Properties. The solution structure is analyzed using the radial pair distribution function (RDF)

$$g(r) = \frac{\rho(r)}{\rho_{\text{bulk}}} \quad (17)$$

where r is the distance from the central atom and $\rho(r)$ and ρ_{bulk} are the local and bulk densities of the surrounding atom, respectively. We define the position of the first peak in the RDF as the equilibrium distance between the corresponding atom pairs. Also, the first and second minimums in the Na–O_w RDF are respectively considered as the boundaries of the first and second solvation shells around Na⁺. The coordination number (CN) of Na⁺ is the number of oxygen atoms (O and O_w) up to the boundary of its first solvation shell. Based on the number of the anions located within the first and second solvation shells of Na⁺, solvation structure is categorized into four kinds: free Na⁺ ions that have no anions in their solvation shells, solvent-separated ion pairs (SSIPs), where at least one anion resides in the second solvation shell of Na⁺ while the first shell is free of anions, contact ion pairs (CIPs), with one anion located in the first solvation shell of Na⁺, and aggregating ion pairs (AGGs), containing more than one anion in the first solvation shell of Na⁺. We calculate the number of anions residing within the two solvation shells of each Na⁺ every 50 ps from the last 5 ns of the production run. The results are then averaged over time and used to calculate the proportions of the different solvation structures.

2.4.3. Vibrational Frequencies. To calculate the vibrational frequencies, the last 25 ps of the simulation trajectories are broken into 10 segments of equal length, and the velocity autocorrelation function (VACF) vs time is calculated for each segment and averaged over all segments. This is done separately for water and ions; i.e., the VACF is averaged once over water molecules and once over Na⁺ and OTF⁻ ions. Then, a one-dimensional discrete Fourier Transform is applied to the VACF, characterizing the vibrational spectra of water and ions.

3. RESULTS AND DISCUSSION

The properties of the studied WiS electrolyte and their sensitivity to the force field parameters are examined below. For this, we start from a base set of force field parameters, listed in Table 1, and vary the parameter values individually to capture their effects on the electrolyte properties.

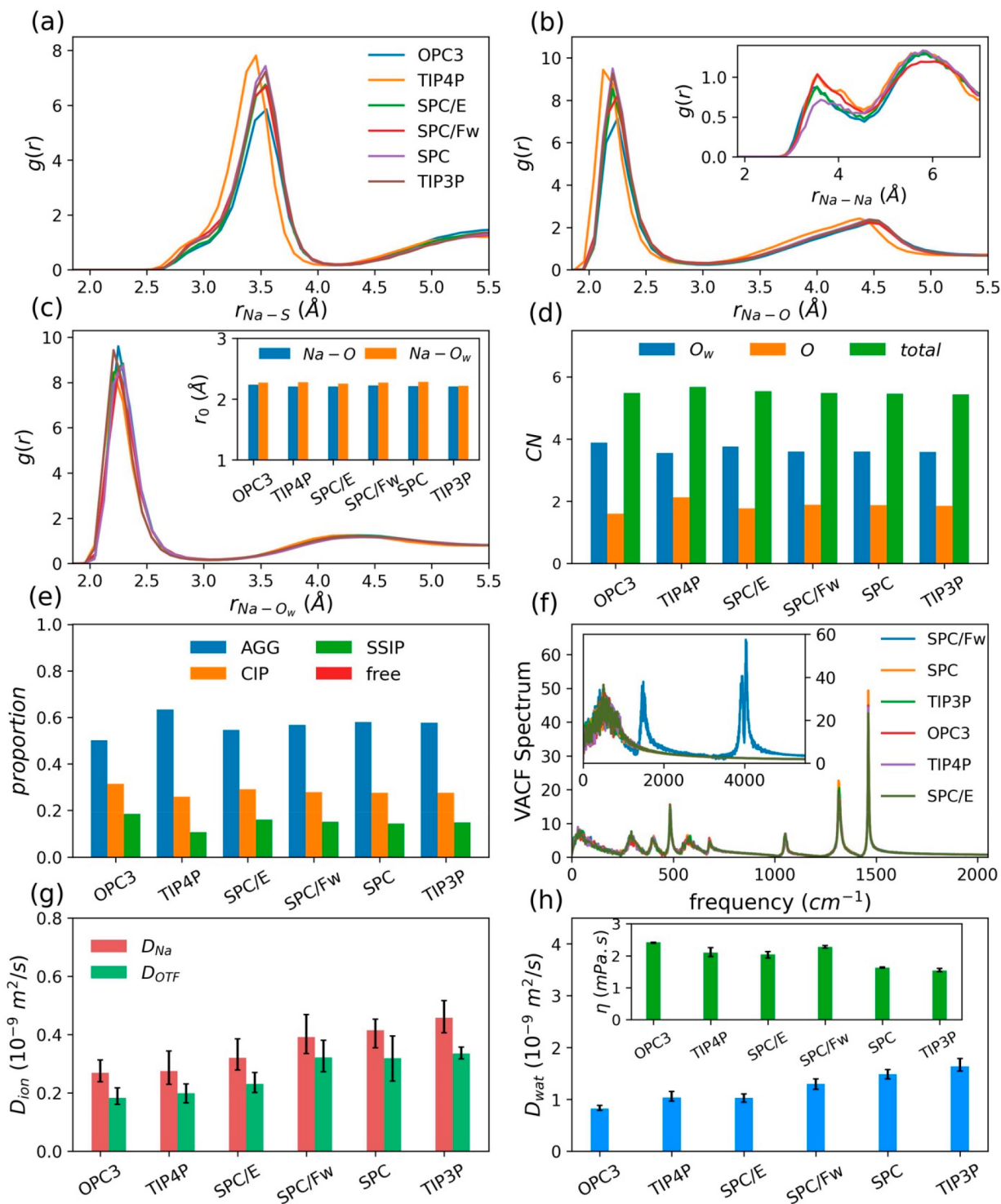


Figure 1. Dependence of the electrolyte properties on water models (results are shown for the BNP force field described in Table 1): (a–c) Radial pair distribution functions (RDFs) of the Na–S, Na–O, Na–Na, and Na–O_w pairs. The inset of panel c shows the positions of the first peaks in the Na–O and Na–O_w RDFs. (d) Total coordination number (CN) of Na⁺ and the average number of Na-coordinated O_w and O atoms. (e) Proportions of the solvation structures described in section 2.4.2 (AGG, aggregates; CIP, contact ion pairs; SSIP, solvent-separated ion pairs; and free, free ions). (f) Vibrational spectra of ions (main panel) and water (inset). (g) Diffusion coefficients of Na⁺ cations, D_{Na} , and the OTF⁻ anions, D_{OTF} . (h) Water diffusion coefficient, D_{wat} and viscosity of the electrolyte, η .

3.1. Nonpolarizable Force Field. In the first step, the nonpolarizable force field (see section 2.1.1) is parametrized using seven water models described in section 2.2.1 (see Table S1). Figure 1 shows that all of these water models produce similar electrolyte properties in terms of radial pair distribution

functions (see panels a–c), coordination environment of cations (see panel d), and proportions of the different solvation structures: free ions, SSIPs, CIPs, and AGGs (see panel e). This indicates that the choice of water model has little impact on the microscopic structure of the WiS electrolyte.

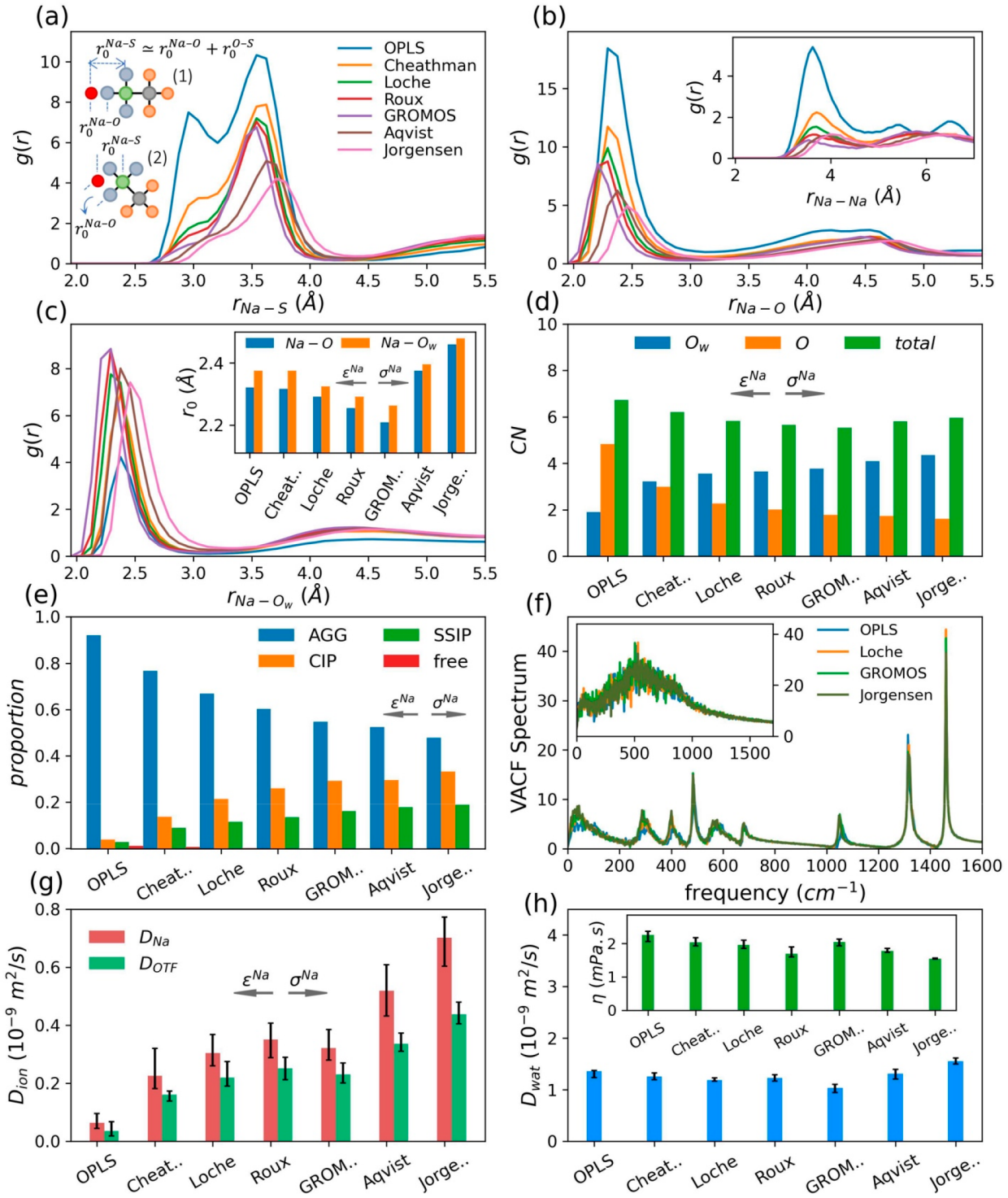


Figure 2. Dependence of the electrolyte properties on the LJ parameters of Na^+ (σ^{Na} and ϵ^{Na} are taken from the literature, see Table S3, and the other parameters are set according to the BNP force field described in Table 1): (a–c) Radial pair distribution functions (RDFs) of the Na–S, Na–O, Na–Na, and Na–O_w pairs. The inset of panel a represents a schematic view of the (1) monodentate and (2) bidentate Na-OTF coordination configurations (Na, O, S, C, and F atoms are shown by red, blue, green, gray, and orange balls, respectively). The inset of panel c shows the positions of the first peaks in the Na–O and Na–O_w RDFs. (d) Total coordination number (CN) of Na⁺ and the average number of Na-coordinated O_w and O atoms. (e) Proportions of the solvation structures described in section 2.4.2 (AGG, aggregates; CIP, contact ion pairs; SSIP, solvent-separated ion pairs; and free, free ions). (f) Vibrational spectra of ions (main panel) and water (inset). (g) Diffusion coefficients of Na⁺ cations, D_{Na^+} and OTF⁻ anions, D_{OTF^-} . (h) Water diffusion coefficient, D_{wat} and viscosity of the electrolyte, η .

Furthermore, all water force field models predict almost the same vibrational frequencies (see Figure 1f). However, the rigid models are not able to capture the O_w–H stretch and H–

O_w–H bending motions (see Figure 1f, inset) because they treat fixed water configuration.

The dependence of the dynamic properties of the electrolyte on the choice of the water model is more pronounced.

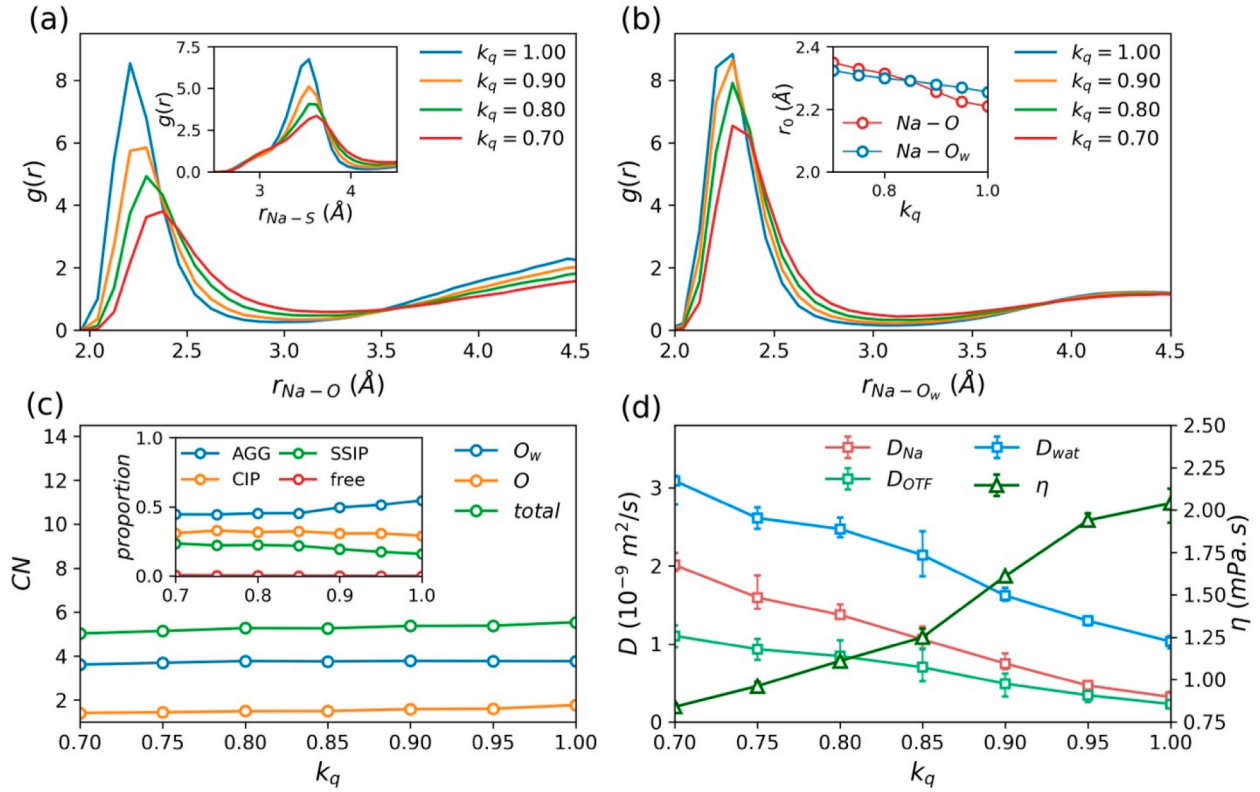


Figure 3. Effects of ionic charge scaling on the properties of the studied WiS electrolyte (results are obtained using the BNP force field described in Table 1): (a, b) Radial pair distribution functions (RDFs) of the Na–O, Na–S, and Na–O_w pairs. The inset of panel b shows the positions of the first peaks in the Na–O and Na–O_w RDFs as a function of the charge scaling factor, k_q (eqs 2 and 3). (c) Total coordination number (CN) of Na⁺ and the average number of Na-coordinated O_w and O atoms as a function of k_q . The inset shows the proportion of different solvation structures (see section 2.4.2) vs k_q . (d) Diffusion coefficients of water and ions (D_{wat} , D_{Na} , and D_{OTF}), and viscosity of the electrolyte, η , as a function of k_q .

According to Figure 1, panels g and h, switching between different water models has a modest impact on the electrolyte viscosity, which itself exhibits an inverse correlation with the diffusion coefficients of water and ions. However, the SPC/Fw model deviates slightly from this trend. Unlike the other models, this model incorporates bending and stretching vibrations in the thermal motions of water molecules, enhancing water mobility and facilitating the movement of ions within the water matrix. As a result, the SPC/Fw model yields higher diffusion coefficients for both water and ions compared to those of the SPC/E and TIP4P models, despite the latter models having slightly lower viscosities. Also, Figure 1h demonstrates that the extremely high salt concentration of the WiS electrolyte results in lower water diffusivity compared to that reported for pure water at the same temperature ($D_{\text{wat}}^{T=333\text{K}} \simeq (4-5) \times 10^{-9} \text{ m}^2/\text{s}$ ^{82,83}). Recognizing the dependence of the dynamic properties on the choice of water model, our results demonstrate that this dependency is negligible for the SPC/E, TIP4P, and OPC3 models, which are known to be more accurate for bulk electrolyte simulations. The quality of the WiS electrolyte simulations therefore has no significant dependence on these water models.

Next, using the previously optimized LJ parameters for Na⁺ listed in Table S3, we investigate the influence of the cation parameters on the electrolyte properties. We note that depending on the values of σ^{Na} and ϵ^{Na} , the Na–S RDF shows one or two distinct peaks (Figure 2a). This indicates that the Na–OTF coordination configuration is sensitive to the LJ parameters of Na⁺. As shown schematically in the inset of

Figure 2a, OTF[−] can coordinate with Na⁺ either monodentately, i.e., with one O atom bound to Na⁺, or bidentately, i.e., with two O atoms bound to Na⁺. In the monodentate configuration, the distance between Na⁺ and S is separated by the bridging O atom as $r_0^{\text{Na-S}} \simeq r_0^{\text{Na-O}} + r_0^{\text{O-S}}$, with $r_0^{\text{Na-O}}$ being the average distance between Na⁺ and its neighboring O atom (i.e., the position of the first peak in the Na–O RDF) and $r_0^{\text{O-S}}$ being the optimal length of the O–S bond, $r_0^{\text{O-S}} = 1.442 \text{ \AA}$ (see Table S4). Therefore, the peak appearing in the Na–S RDF at $r_0^{\text{Na-O}} + r_0^{\text{O-S}}$ (here, around 3.5–3.75 Å) represents the monodentately coordinated ion pairs. In the bidentate configuration, Na⁺ gets closer to the S atom of its coordinated OTF[−] than in the monodentate configuration (Figure 2a, inset). Thus, the bidentately coordinated ion pairs can be recognized by a peak appearing in the Na–S RDF at $r_0^{\text{Na-S}} < r_0^{\text{Na-O}} + r_0^{\text{O-S}}$. Figure 2a shows that the monodentate configuration occurs in all of our simulations, but the existence of bidentately coordinated ion pairs strongly depends on the LJ parameters of Na⁺. In practice, the Na–OTF coordination configuration is mainly determined by the balance between the attractive LJ and repulsive Coulomb contributions to the interactions between Na⁺ and S. Due to the shorter distance and thus stronger electrostatic repulsion between these two atoms in the bidentate configuration, this configuration is less stable than the monodentate one and accounts for a smaller proportion of ion pairs (Figure 2a). However, using the parameters that model stronger LJ interactions for Na⁺, e.g., the OPLS parameters, makes the ion pair configuration more stable and increases the occurrence of the bidentate

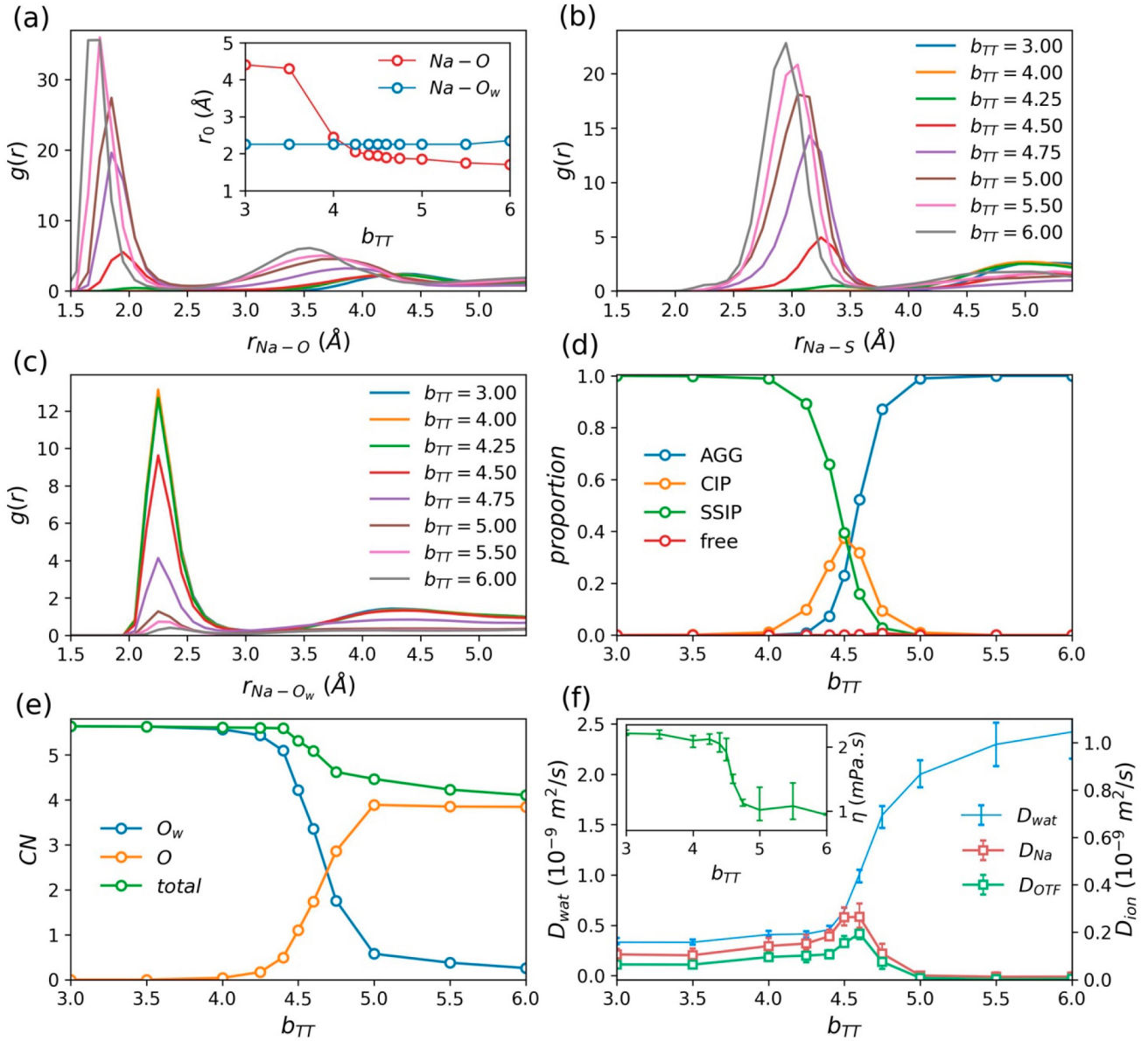


Figure 4. Dependence of the electrolyte properties on the damping parameter b_{TT} , used in the Tang–Toennies function given by eq 12 (other parameters are set according to the BPP force field described in Table 1): (a–c) Radial pair distribution functions (RDFs) of the Na–O, Na–S, and Na– O_w pairs. The inset shows the positions of the first peaks in the Na–O and Na– O_w RDFs. (d) Proportions of different solvation structures described in section 2.4.2 (AGG, aggregates; CIP, contact ion pairs; SSIP, solvent-separated ion pairs; and free, free ions). (e) Total coordination number (CN) of Na^+ and the average number of Na-coordinated O_w and O atoms. (f) Diffusion coefficients of water and ions, D_{wat} , D_{Na} , and D_{OTF} . The inset shows the viscosity of the electrolyte, η .

configurations (Figure 2a). This effect is manifested in the increased height of the peak appearing in the Na–S RDF at $r^{\text{Na-S}} < r_0^{\text{Na-O}} + r_0^{\text{O-S}}$ (see Figure 2a).

The dependence of the average distance between Na^+ ions and their neighboring oxygen atoms in water molecules and OTF[−] anions, $r_0^{\text{Na-O}_w}$ and $r_0^{\text{Na-O}}$, on the LJ parameters of Na^+ is demonstrated in the inset of Figure 2c. Moving from right to left on the x axis, the parameter sets represent smaller values of σ^{Na} and larger values of ϵ^{Na} (Table S3). A smaller σ^{Na} , indicating a smaller radius of the soft repulsive core of the LJ potential, tends to decrease the Na–O and Na– O_w distances. Conversely, a larger ϵ^{Na} tends to increase these distances due to the steeper repulsive part of the corresponding LJ potentials. Furthermore, an increase in ϵ^{Na} increases the occurrence of the bidentate coordination configurations, as discussed above,

which slightly increases the average Na–O distance. The reason is that the optimal Na–O distance in the bidentate configuration is slightly larger than that in the monodentate one, which could be attributed to the strong Na–S Coulomb repulsion in the bidentate configuration. The competition of the above factors results in nonmonotonic variations of $r_0^{\text{Na-O}}$ and $r_0^{\text{Na-O}_w}$ with the LJ parameters of Na^+ , as shown in the inset of Figure 2c.

According to Figure 2d, all of the examined LJ parameters provide almost the same total coordination number of $\text{CN} \simeq 6$ for Na^+ ions. However, the LJ parameters with larger σ^{Na} and smaller ϵ^{Na} lead to smaller Na–O coordination numbers (Figure 2d). This indicates a higher degree of salt dissociation, which manifests itself in an increased proportion of CIPs and SSIPs at the expense of the proportion of AGGs (Figure 2e).

Considering that the aggregated ion pairs diffuse together as a complex, the reduced proportion of AGGs has two notable effects on ion diffusivities. First, it leads to a more independent diffusion of cations and anions, thereby increasing the difference between their respective diffusion coefficients (Figure 2g). Second, it results in a decrease in the average size of the diffusing ion species, leading to a significant increase in their diffusion coefficients (Figure 2g). For example, the diffusion coefficients of both cations and anions obtained using the Jorgensen parameters for Na^+ interactions are more than 10 times larger than those obtained using the OPLS parameters. Therefore, the meticulous selection of the LJ parameters for cations is a crucial step in molecular dynamics modeling of WiS solutions, as it strongly influences both the solvation structure and dynamics of the salt ions. Conversely, the selection between the studied Na^+ parameters has a comparatively minor impact on the electrolyte viscosity and, consequently, water diffusivity (Figure 2h).

Figure 2g provides a rough idea of how fast monatomic ions diffuse in a WiS electrolyte. The LJ parameters of the monatomic ions Li^+ , Na^+ , and K^+ in the previous simulations typically follow the orders $\sigma_{\text{Li}^+} < \sigma_{\text{Na}^+} < \sigma_{\text{K}^+}$ and $\epsilon_{\text{Li}^+} > \epsilon_{\text{Na}^+} > \epsilon_{\text{K}^+}$.^{84,85} Although the LJ parameters examined in this study are all optimized for Na^+ , they exhibit a similar trend of variations (see Figure 2 and Table S3). Our results, therefore, indirectly indicate a relationship between the size of the ions and their diffusivity in the WiS electrolyte, $D_{\text{Li}^+} < D_{\text{Na}^+} < D_{\text{K}^+}$ (see Figure 2g), as previously reported for low salt concentrations (salt-in-water solutions).^{70,86,87} For a more accurate assessment, of course, the force field parameters should first be optimized for each ion species.

3.2. Uniform Ionic Charge Scaling in Nonpolarizable Force Fields. Based on a mean-field approach, the ionic charge scaling using the factor k_q in eq 3 can account for the effective polarization within nonpolarizable force field methods. Figure 3a,b indicate that applying ionic charge scaling leads to a more disordered solvation shell around Na^+ , which is manifested in the widening and lowering of the first peaks in the Na–O and Na– O_w RDFs. However, the ionic charge scaling has only a minor effect on the other properties of the solvation structure, such as the equilibrium distance between Na^+ and its nearest atoms, $r_0^{\text{Na}-\text{O}}$ and $r_0^{\text{Na}-\text{O}_w}$ (Figure 3b, inset), the coordination number of Na^+ (Figure 3c), and the Na-OTF pair configurations (see the inset of Figure 3a and the discussion in section 3.1). Furthermore, the ionic charge scaling slightly enhances salt dissociation, leading to a gentle increase in the proportion of CIPs and SSIPs at the expense of the proportion of AGGs, while the number of free cations remains almost zero (Figure 3c, inset). In contrast, the dynamic properties of the solution are strongly dependent on the charge scaling factor. As shown in Figure 3d, the viscosity of the solution decreases for a smaller scaling factor, primarily due to the reduced ion–ion and ion–water electrostatic interactions. This decreased viscosity, in turn, leads to a faster diffusion of both water and ions, as demonstrated in Figure 3d. As a result, the ionic charge scaling method can be effective when the simulation yields a lower diffusion rate than expected, while the solvation structure does not need further adjustments.

An important point to note here is that adjusting the charge scaling factor alone is insufficient to correctly predict the overall electrolyte properties, as it can result in correct diffusion coefficients but incorrect solution structure. For

example, Figure S4 shows the results obtained using three different sets of force field parameters, where k_q is adjusted such that the corresponding simulations yield the same diffusion coefficients for Na^+ . These force field parameters, however, lead to completely different solvation structures around Na^+ and different electrolyte viscosities (see SI section D for more details). Therefore, the charge scaling factor can be used as an additional force field parameter to effectively adjust ion diffusion, while the microscopic structure of the electrolyte should be modified via other force field parameters. The same effect has already been observed for charge scaling in ionic liquids.⁸⁸

3.3. Partially Polarizable Force Field. We explicitly model dynamic polarization at various levels using Drude oscillators (section 2.1.2). First, Drude particles are attached to Na^+ and the atoms of OTF^- while water is modeled using the nonpolarizable SPC/E model. The resulting force field is termed a “partially polarizable” force field. We start with the BPP force field parameters listed in Table 1 and vary the parameter values that adjust Drude interactions, i.e, k_D , α^{Na} , b_{TT} , c_{TT} , k_a^{OTF} , and a (see section 2.2.2), to investigate their effects on the electrolyte properties. Figure 4 shows the results for b_{TT} . The results for the other Drude parameters are presented in the SI, section E, as they have similar effects on the electrolyte properties as b_{TT} .

Figures 4 and S5–S9, panel b, show that all the considered values of the Drude parameters predict a dominant monodentate Na-OTF coordination (see the discussion in section 3.1), indicating that Drude parameters have little influence on the coordination configuration of Na-OTF ion pairs. The equilibrium distance between Na^+ and its nearest water oxygens, $r_0^{\text{Na}-\text{O}_w}$, is also nearly independent of the Drude parameters (Figures 4 and S5–S9, the inset of panel a). The Na–O equilibrium distance, $r_0^{\text{Na}-\text{O}}$, however, increases with decreasing b_{TT} or increasing either k_D , α^{Na} , or c_{TT} (see Figures 4 and S5–S9, inset of panel a). Furthermore, the coordination number of Na^+ ions, the abundance of each solvation structure (section 2.4.2), and the dynamic properties of the electrolyte are strongly dependent on the Drude parameters (Figures 4 and S5–S9, panels d–f). Our results indicate that increasing b_{TT} or decreasing either α^{Na} , α^{OTF} , k_D , or c_{TT} reduces the occurrence of SSIPs (Figures 4 and S5–S9, panel d) and increases the number of Na-coordinated OTF^- anions (Figures 4 and S5–S9, panel e), while the water coordination to Na^+ decreases (see Figures 4 and S5–S9, panel e). In the absence of free Na^+ ions, this corresponds to a decrease in the NaOTF dissociation degree. For sufficiently small values of b_{TT} or sufficiently large values of either k_D , α^{Na} , or c_{TT} , all ion pairs are solvent-separated (fully dissociated salt), and the Na-water coordination number is around 5.6 (see Figures 4 and S5–S7, panels d and e), which is close to what ab initio MD predicts at the same temperature at low salt concentrations.⁸⁹ As the degree of salt dissociation decreases due to the above-mentioned variations in the Drude parameters, the proportion of AGGs increases, but the proportion of CIPs first increases and then starts to decrease (see Figures 4 and S5–S9, panel d). The reason is that the dissociation occurs from AGG to SSIP configurations through CIP, and the conversion from CIP to SSIP occurs faster than AGG to CIP at the parameters that lead to a higher dissociation degree.

As demonstrated in Figures 4 and S5–S9, panels d and f, at lower degrees of salt dissociation, the electrolyte exhibits lower viscosity. This can be attributed to the reduced coordination of

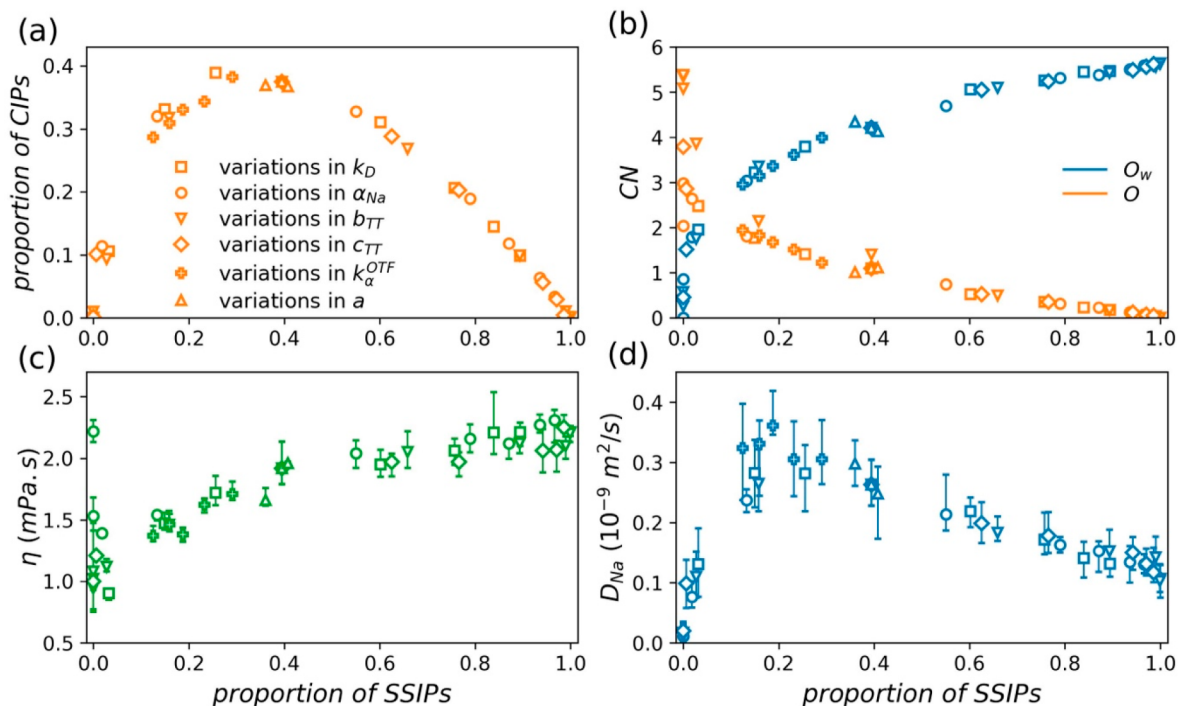


Figure 5. Effects of the studied Drude parameters on the Na-OTF dissociation degree (represented by the proportion of solvent-separated ion pairs, SSIPs) and thereby on the electrolyte properties: (a) proportion of contact ion pairs, CIPs, (b) Na–O and Na– O_w coordination numbers, (c) viscosity of the electrolyte, η , and (d) diffusion coefficient of Na^+ , D_{Na} . Except for the modified Drude parameter, all force field parameters are set according to the BPP force field described in Table 1.

water molecules with the charged species and the resulting less dispersed distribution of charge.⁹⁰ Consequently, systems with lower degrees of salt dissociation demonstrate higher water diffusivity (see Figure 4, panels d and f). The relationship between the degree of salt dissociation and ion diffusivity is, however, more complex. On one hand, the aggregation of ions decreases the electrolyte viscosity (as discussed above), which tends to raise ion diffusivity. On the other hand, it increases the size of the diffusing ion species, which tends to lower ion diffusivity. These two competing factors cause nonmonotonic variations in the diffusion coefficients of both cations and anions (see Figure 4, panel f). At high degrees of salt dissociation, where the SSIP configuration is dominant, any change in Drude parameters that decreases the degree of salt dissociation leads to an increase in both D_{Na} and D_{OTF} (see Figure 4, panels d and f). This suggests that in electrolytes where dissociated salt ions predominate, the primary factor influencing ion diffusivity is the electrolyte viscosity. In such electrolytes, the diffusion coefficients of water and ions exhibit similar trends with relatively small deviations, suggesting that most of the water molecules are involved in the solvation of ions and codiffuse with them. At lower degrees of salt dissociation, where the AGG configuration prevails, both D_{Na} and D_{OTF} begin to decrease with a decrease in the degree of salt dissociation, despite the solution becoming less viscous and D_{wat} continuing to increase (see Figure 4, panels d and f). In this case, the primary factor influencing ion diffusivity is the increased average size of the aggregates. At these low degrees of salt dissociation, the majority of water molecules can freely diffuse without significant influence from the ions, as evidenced by the notable increase of the water diffusion coefficient (see Figure 4f). Close to the lower or upper edges of the varying Drude parameter range, i.e., when the ions are either fully

associated or fully dissociated (see Figures 4 and S5–S7, panel d), the solvation structure and, subsequently, the electrolyte viscosity and diffusion coefficients exhibit minor changes with variations in the Drude parameters (see Figures 4 and S5–S7, panel d–f). The only exception is a large viscosity change at small α_{Na} (see panel f of Figure S6), which can be attributed to the changes in the number of Na-coordinated anions (see panel e of Figure S6).

Figure 4, panels d and f, demonstrate the significance of salt dissociation degree in determining the performance of WiS electrolytes in battery applications. The key objective in these applications is to maximize ion diffusivity while ensuring the active participation of water molecules in the solvation shells of ions. The latter aspect is particularly important as it preserves the large electrochemical stability window of the electrolyte, which, together with the increased ion mobility, contributes to the overall performance of the battery. According to Figures 4 and S5–S9, panels d and f, the maximal ion diffusivity in the studied WiS electrolyte occurs when SSIPs and AGGs have almost equal proportions, while the proportion of CIPs is at its maximum. In this configuration, the diffusion coefficient of water has not yet deviated significantly from the diffusion coefficients of ions (Figure 4f), indicating that a substantial proportion of water molecules are still strongly attracted to ions. These findings highlight the importance of the dissociation characteristics of salt ions as a key factor in optimizing WiS electrolytes for batteries. Moreover, they emphasize the crucial influence of the Drude parameters on the salt dissociation and, consequently, on the electrolyte properties in MD simulations of WiS solutions.

Figure 5 demonstrates that the studied Drude parameters strongly control the degree of salt dissociation, which in turn influences the other properties of the electrolyte. However, the

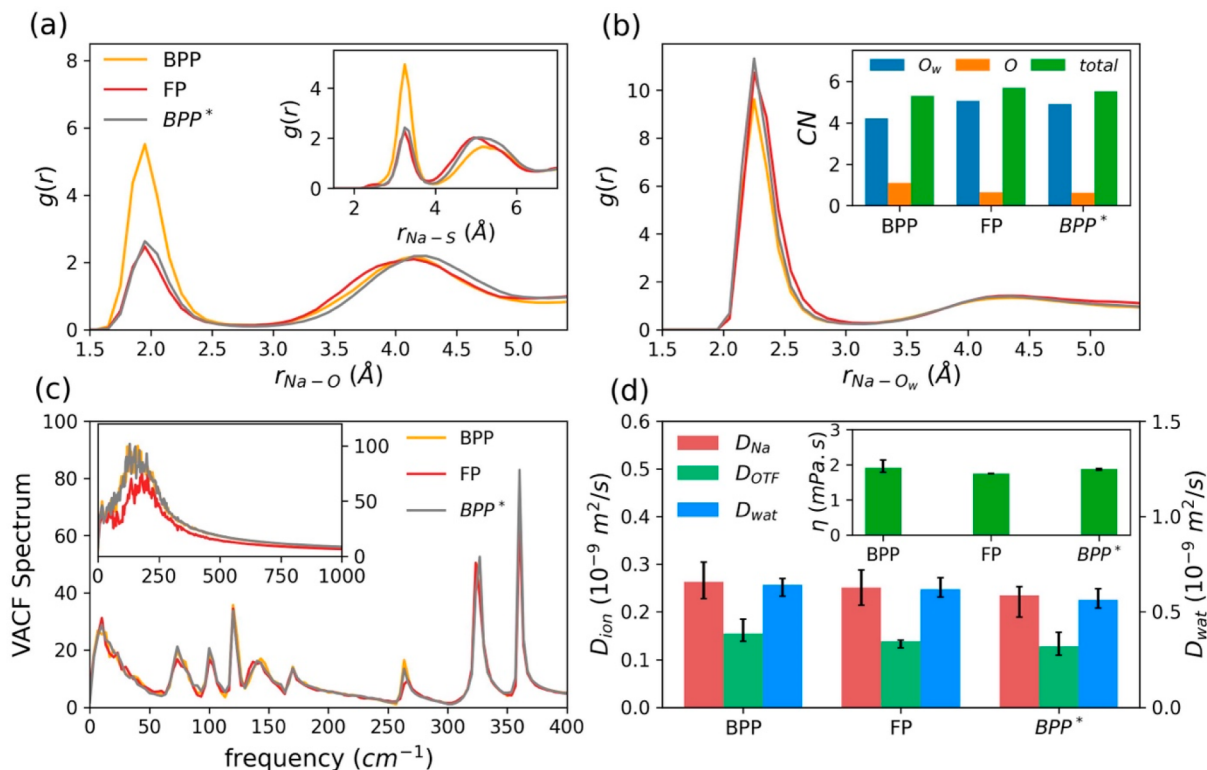


Figure 6. Electrolyte properties obtained using different polarizable force fields: BPP and FP force fields, which are described in Table 1, and the BPP* force field, which is identical to the BPP except that b_{TT} is set to 4.44. (a, b) Radial pair distribution functions (RDFs) of the Na–O, Na–S, and Na–O_w pairs. The inset of panel b shows the total coordination number (CN) of Na⁺ and the average number of Na-coordinated O_w and O atoms. (c) Vibrational spectra of ions (main panel) and water (inset). (d) Diffusion coefficients of water and ions: D_{wat} , D_{Na} , and D_{OTF} . The inset shows the viscosity of the electrolyte, η .

direct influence of the Drude parameters on the solvation structure and dynamic properties is negligible. In other words, different sets of Drude parameters that yield the same degree of salt dissociation (or the same proportion of SSIPs in Figure 5) result in nearly identical electrolyte properties. Thus, it is not essential to optimize each of the Drude parameters separately. Instead, modifying a single parameter during the force field optimization process would suffice to achieve a desirable degree of salt dissociation. While α^{Na} and k_{D} are also suitable options, we recommend b_{TT} as the best choice for this purpose, as it can be easily adjusted to reproduce a variety of solution structures without compromising simulation stability. The scaling of anion polarizability can be safely disregarded, as it has a minor influence on the electrolyte properties, especially on D_{Na} and η (see Figure S8). The Thole damping parameter a , which is varied in a small range of 2.1–2.8 due to simulation stability issues, has negligible effects on electrolyte properties (see Figure S9) and can take the standard value of 2.6. Similarly, a moderate impact has been reported for the Thole damping function in ionic liquid simulations.⁵⁸

3.4. Fully Polarizable Force Field. Finally, the SWM4-NDP water model (section 2.2.1) is employed to set up a fully polarizable simulation using the FP force field parameters listed in Table 1. This simulation yields almost the same ion diffusivity, viscosity, and vibrational frequencies as the partially polarizable simulation with the BPP force field parameters (see Table 1), but it shows a different number for Na-coordinated atoms. We note that this difference can be reduced by adjusting the BPP force field parameters. For example, the modified BPP force field with $b_{\text{TT}} = 4.44$, denoted as BPP* in

Figure 6, can reproduce the results well from the FP force field. It indicates that the fully polarizable and the partially polarizable force fields can model the studied WiS electrolyte equally well. However, the SWM4-NDP water model in the fully polarizable force field requires more particles and bonds, thus causing a higher computational effort, and leads to more severe stability issues (see the discussion in section 3.5). We, therefore, strongly recommend using partially polarizable force fields for future WiS electrolyte studies.

3.5. Simulation Stability and Runtime. As mentioned in section 2.1.2, maintaining simulation stability is an important challenge when a Drude polarizable force field is used. To maintain simulation stability, in addition to applying appropriate damping functions to short-distance electrostatic interactions (see eqs 10 and 12), a sufficiently small time step is necessary. For example, time steps larger than 0.5 and 0.4 fs, respectively, cause instability in the BPP and FP polarizable simulations (both described in Table 1), while the non-polarizable simulations remain stable with a much larger time step of 2 fs. We note that increasing the DP–DC force constant, k_{D} , can improve the stability of simulations with Drude oscillators and allow for a larger time step. For example, the time steps required for stable partially polarizable simulations with $k_{\text{D}} = 1000$ kcal/mol \AA^2 , $k_{\text{D}} = 2000$ kcal/mol \AA^2 , and $k_{\text{D}} = 4000$ kcal/mol \AA^2 are, respectively, 0.15, 0.5, and 0.7 fs. For k_{D} smaller than 1000 kcal/mol \AA^2 , the simulation persists as unstable even though the time step is as small as 10^{-2} fs. Furthermore, a small k_{D} narrows the applicable range of the other Drude parameters (i.e., α^{Na} , α^{OTF} , k_{D} , b_{TT} ,

and c_{TT}) for stable simulations. It is, therefore, advantageous to set k_{D} to large enough values.

Another problem reported for Drude polarizable simulations is the flying ice cube artifact,⁹¹ i.e., irreversible transfer of linear momentum to the center of mass of the system. This artifact can be identified by an unphysically fast change in the mean squared displacement of randomly walking atoms, which usually increases linearly with time. Although the flying ice cube problem is mostly reported for simulations where temperature is kept constant by velocity rescaling^{91–93} (e.g., the Berendsen thermostat), this problem can occur in the presence of Drude oscillators even with the Nose-Hoover thermostat. The reason is that the two separate thermostats applied to the atomic and dipolar subsystems (section 2.3) are insensitive to how the kinetic energy is partitioned among the degrees of freedom. It causes an accumulation of numerical errors along MD trajectories and may result in this artifact at a certain point.⁶⁷ For the partially polarizable force field, we encounter the flying ice cube problem only with $k_{\text{D}} = 1000$ kcal/mol \AA^2 , which is the smallest k_{D} for a stable simulation. In the presence of SWM4-NDP water molecules, however, this problem becomes more severe because another separate thermostat is applied to the water molecules (section 2.3). To avoid this problem, the linear momentum of the system should be zeroed by subtracting the center-of-mass velocity from the velocity of each atom every time step. The correction assumes a uniform distribution of the spurious kinetic energy over all atoms. For example, the flying ice cube artifact occurs in the BPP' simulation described in Table 2. However, the MSD vs time curve obtained from the same force field but after the linear momentum correction (the BPP'' simulation) is perfectly linear (see Figure 7, inset).

Table 2. Force Field Parameters Used for Performance Testing

BNP	base nonpolarizable force field (parameters are given in Table 1)
BNP'	the same parameters as in the BNP except that SPC/E water is replaced with TIP4P water
BPP	base partially polarizable force field (parameters are given in Table 1)
BPP'	the same parameters as in the BPP simulation except that k_{D} is set to 1000 kcal/mol \AA^2
FP	fully polarizable force field (parameters are given in Table 1)

In addition to the accuracy of the force field and the stability of the simulation, the computational cost is also an important factor in the appropriate choice of a force field. Figure 7 shows the runtimes for force field simulations considering different levels of dynamic polarization, as described in Table 2. All of these simulations are run for 24 ns on the bwForCluster JUSTUS2 HPC cluster using 48 CPU cores. The time step is set to 2 fs for the BNP and BNP' simulations, while shorter time steps of 0.5, 0.15, and 0.4 fs are, respectively, used for the BPP, BPP', and FP simulations. According to Figure 7, the BNP simulation requires the lowest computational cost. The BNP' simulation is a bit slower due to the additional massless fourth site in the TIP4P water model. The reduced time step and the increased number of particles and bonds have significantly increased the runtime of the BPP simulation compared to the BNP and BNP' simulations. The BPP' simulation gets even slower than the BPP because of its very small time step. In the case of the FP simulation, water molecules have four sites and one Drude particle, which

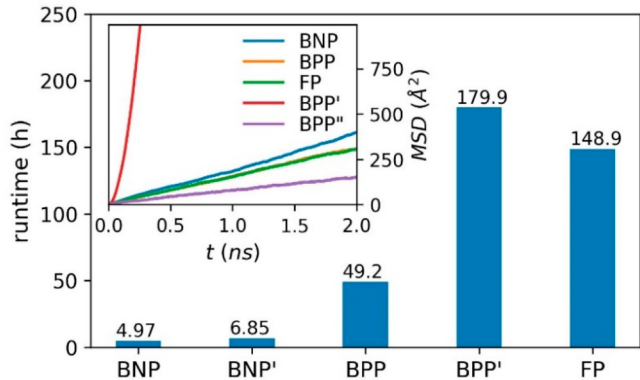


Figure 7. Runtimes for the simulations described in Table 2 (main panel) and the resulting plot of the mean-squared-displacement vs time (inset). The red line in the inset shows the results from the BPP' force field with the flying ice cube effect, and the purple line shows the results from the same force field when this effect is avoided by zeroing the linear momentum every time step.

increases the number of particles and bonds compared to the BPP simulation and, consequently, makes the simulation much slower than the BPP. It is worth noting that if one uses $k_{\text{D}} = k_{\text{D}}^{\text{ow}} = 1000$ kcal/mol \AA^2 in the fully polarizable simulation, a time step as small as 0.01 fs can stabilize the simulation. Using this setup, the simulation will take about 250 days.

3.6. WiS Electrolytes in Rechargeable Batteries. The results presented in this paper not only compare the possible strategies for inclusion of polarization effects in the molecular modeling of WiS electrolytes, but also provide a general insight into how WiS electrolytes work in rechargeable batteries. Most interestingly, our results indicate the existence of an optimal degree of salt dissociation where ion diffusivity is maximum (see Figures 4 and S5–S9). Thus, in order to achieve the maximum efficiency of WiS electrolytes in rechargeable batteries, the degree of salt dissociation and hence the solvation energy of the ions should be optimized. In fact, weak ion solvation reduces battery performance through the formation of aggregates, while excessive ion solvation is also undesirable not only because of the increased viscosity of the electrolyte, but also because it prevents ion desolvation at the electrodes and disrupts the intercalation process. Our results also indicate that, depending on the values set for the force field parameters (and assuming that the fully aggregated ionic structure never occurs in reality), the diffusion coefficient of Na^+ in the studied WiS solution is in the range of 10^{-10} to 10^{-9} m^2/s , which is comparable to the values reported for Na^+ diffusion in organic electrolytes conventionally used in batteries.^{24,94–96} Experimental measurements^{97–99} and numerical calculations^{100–104} indicate that the diffusion coefficient of Li^+ is almost in the same range (sometimes even lower) in different battery electrolytes. This means that, with WiS electrolytes, water can be used in batteries as a safe, available, and environmentally friendly solvent, while ion diffusivity, which is expected to be greatly reduced at high salt concentrations,²⁴ is still within the working range of batteries.

4. CONCLUSION

Molecular modeling of highly concentrated electrolytes, such as water-in-salt (WiS) solutions, requires a proper inclusion of polarization contributions to atomic interactions. In this work, a NaOTF WiS electrolyte is modeled using classical molecular

dynamics (MD) simulations with accounting for polarization effects at four levels. We consider first a nonpolarizable all-atom force field with Lennard-Jones (LJ) and Coulomb potential interactions where an effective polarization is implicitly accounted for in the LJ interaction parameters. Second, on top of the nonpolarizable force field, uniformly scaled ionic charges are considered, which supposedly account for average polarization in a mean-field approximation. Third, a partially polarizable force field is considered to explicitly model the polarizability of salt ions via Drude oscillators while using the nonpolarizable SPC/E water model. Finally, we consider a fully polarizable force field using Drude oscillators for both salt ions and water molecules. The electrolyte properties and their dependence on the force field parameters are probed by varying the parameter values within a range in which the simulations remain stable.

Our study highlights the crucial role of the LJ parameters of monatomic ions (here, Na^+) in determining the structure of the WiS electrolyte and its dynamic properties. In particular, we show the substantial impact of these parameters on the cation–anion coordination configuration and ion diffusivity. On the other hand, our simulations demonstrate that the well-accepted water models yield similar properties for the studied WiS solution, suggesting that the quality of the electrolyte simulation has no significant dependence on the choice of water model. Moreover, we observe that uniform scaling of ionic charges significantly affects the dynamic properties of the electrolyte but has a minimal impact on its structure. This implies that ionic charge scaling is mainly useful for fine-tuning the dynamic properties while preserving the overall structure of the solution.

The introduction of Drude oscillators extends the number of force field parameters for adjusting the properties of the electrolyte. The Drude parameters primarily control the electrolyte properties by modifying the degree of salt dissociation, while having a negligible direct impact on the other properties. Therefore, for force field optimization, modifying only one of the Drude parameters (preferably the Tang–Toennies damping parameter) would suffice to effectively adjust salt dissociation. Our results indicate a complex relationship between the degree of salt dissociation and dynamic properties of the electrolyte. Dissociation of ions reduces the number of aggregates, which tends to raise ion diffusivity, while resulting in a larger electrolyte viscosity, which tends to reduce ion diffusivity. When the salt ions are either fully associated or fully dissociated, ion diffusivity is almost independent of Drude parameters. When the salt ions are partly dissociated, however, the simultaneous action of the above factors causes nonmonotonic variations in the ion diffusion coefficient with the degree of salt dissociation and, consequently, with Drude parameters. For the studied WiS electrolyte, the maximum Na^+ diffusivity occurs when solvent-separated ion pairs and aggregates have nearly equal proportions while the proportion of contact ion pairs is at a maximum.

To ensure the stability of Drude polarizable simulations, it is necessary to appropriately dampen short-distance dipolar interactions and employ a sufficiently small time step. Nevertheless, the numerical errors associated with the dual Nose-Hoover thermostat typically used in such simulations can still arise and lead to another technical problem known as flying ice cube, which must be avoided by zeroing the linear momentum every time step. Our results indicate that

simulation instability and flying ice cube issues are more pronounced when Drude particles are weakly bound to their core atoms. This implies the importance of applying a sufficiently stiff harmonic bond between Drude particles and their cores. Based on our simulations, we recommend using a bond constant of $k_{\text{D}} = 2000 \text{ kcal/mol \AA}^2$ in the WiS electrolyte simulations, which is larger than the typical value used in Drude polarizable force fields ($k_{\text{D}} = 1000 \text{ kcal/mol \AA}^2$).

Finally, we show that the partially polarizable and fully polarizable force fields (which are explicitly polarized salt ions in the nonpolarizable SPC/E and polarizable SWM4-NDP water models, respectively) can model the studied WiS electrolyte equally well. However, the SWM4-NDP water model requires more particles and bonds, thus causing a higher computational effort, and leads to more severe stability issues due to the separate thermostat applied to water molecules. We therefore strongly recommend combining Drude polarizable force fields with nonpolarizable water models, such as SPC/E, in the molecular modeling of WiS electrolytes.

AUTHOR INFORMATION

Corresponding Author

Majid Rezaei – *Institute of Theoretical Chemistry, Ulm University, 89081 Ulm, Germany*;  orcid.org/0000-0003-2844-2313; Email: majid.rezaei@uni-ulm.de

Authors

Sung Sakong – *Institute of Theoretical Chemistry, Ulm University, 89081 Ulm, Germany*;  orcid.org/0000-0001-9777-7489

Axel Groß – *Institute of Theoretical Chemistry, Ulm University, 89081 Ulm, Germany; Helmholtz Institute Ulm (HIU) for Electrochemical Energy Storage, 89069 Ulm, Germany*;  orcid.org/0000-0003-4037-7331

Notes

The authors declare no competing financial interest.

ACKNOWLEDGMENTS

This work was funded by the Deutsche Forschungsgemeinschaft (DFG, German Research Foundation) under Project ID 390874152 (POLiS Cluster of Excellence). Computer time provided by the state of Baden-Württemberg through bwHPC and the German Research Foundation (DFG) under grant no INST 40/575-1 FUGG (JUSTUS 2 cluster) is gratefully acknowledged. This work contributes to the research performed at Center for Electrochemical Energy Storage Ulm-Karlsruhe (CELEST).

NOMENCLATURE

U = Potential energy

ε = Lennard-Jones interaction strength
 σ = Lennard-Jones minimum separation distance
 r = The distance from an atom or between two atoms
 q = Atomic (partial) charge
 k_q = Ionic charge scaling factor
 ε_0 = Vacuum permittivity
 w = Weighting coefficient for pairwise energy between atoms in the same molecule
 k_b = Bond constant
 k_θ = Angle constant
 k_m = Dihedral force constants
 r_0 = Optimal bond length
 θ_0 = Valence angle
 φ_0 = Valence dihedral angle
 V_D = Harmonic potential between a Drude particle and its respective core
 k_D = Bond constant between a Drude particle and its respective core
 r_D = The distance between a Drude particle and its respective core
 q_D = Drude charge representing an induced dipole on a polarizable atom
 m_D = Mass of the Drude particle
 α = Atomic polarizability
 q' = Nonpolarizable part of the charge on a Drude core
 k_{LJ} = Scaling factor for Lennard-Jones interactions between two polarizable fragments
 \bar{q} = The net charge of a polarizable fragment
 $\bar{\alpha}$ = Molecular polarizability of a polarizable fragment
 $\bar{\mu}$ = Dipole moment of a polarizable fragment
 r_0 = Equilibrium distance between the centers of mass of two polarizable fragments
 $T(r)$ = Thole damping function
 a = Thole damping parameter
 $f_{TT}(r)$ = Tang-Toennies (TT) damping function
 b_{TT} and c_{TT} = Tang-Toennies damping parameters
 t = Time
 dt = Time step
 D = Diffusion coefficient
 V = Volume of the simulation box
 $P_{\alpha\beta}$ = Stress in the $\alpha\beta$ plane
 $g(r)$ = Radial pair distribution function
 $r_{1,2}$ = Positions of the first and the second peaks in the radial pair distribution function
 ρ = Density
 k_α^{OTF} = The scaling factor applied to the polarizabilities of the atoms in OTF⁻
WiS = Water-in-Salt
DP = Drude particle
DC = Drude core
CN = Coordination number
VACF = Velocity autocorrelation function
RDF = Radial distribution function
MSD = Mean squared displacement
AGG = Aggregate
CIP = Contact ion pair
SSIP = Solvent-separated ion pair
BNP = Base nonpolarizable (force field)
BPP = Base partially polarizable (force field)
FP = Fully polarizable (force field)
O_w and H = Water oxygen and hydrogen
O, S, C, and F = OTF⁻ oxygen, sulfur, carbon, and fluorine

REFERENCES

- (1) Choi, S.; Wang, G. Advanced Lithium-Ion Batteries for Practical Applications: Technology, Development, and Future Perspectives. *Advanced Materials Technologies* **2018**, *3* (9), 1700376.
- (2) Janek, J.; Zeier, W. G. A solid future for battery development. *Nature Energy* **2016**, *1* (9), 16141.
- (3) Kalhoff, J.; Eshetu, G. G.; Bresser, D.; Passerini, S. Safer Electrolytes for Lithium-Ion Batteries: State of the Art and Perspectives. *ChemSusChem* **2015**, *8* (13), 2154–2175.
- (4) Elia, G. A.; Marquardt, K.; Hoepfner, K.; Fantini, S.; Lin, R.; Knipping, E.; Peters, W.; Drillet, J.-F.; Passerini, S.; Hahn, R. An Overview and Future Perspectives of Aluminum Batteries. *Adv. Mater.* **2016**, *28* (35), 7564–7579.
- (5) Jäckle, M.; Helmbrecht, K.; Smits, M.; Stottmeister, D.; Groß, A. Self-diffusion barriers: possible descriptors for dendrite growth in batteries? *Energy Environ. Sci.* **2018**, *11* (12), 3400–3407.
- (6) Armand, M.; Endres, F.; MacFarlane, D. R.; Ohno, H.; Scrosati, B. Ionic-liquid materials for the electrochemical challenges of the future. *Nat. Mater.* **2009**, *8* (8), 621–629.
- (7) Buchner, F.; Forster-Tonigold, K.; Bozorgchenani, M.; Gross, A.; Behm, R. J. Interaction of a Self-Assembled Ionic Liquid Layer with Graphite(0001): A Combined Experimental and Theoretical Study. *J. Phys. Chem. Lett.* **2016**, *7* (2), 226–233.
- (8) Kim, H.; Hong, J.; Park, K.-Y.; Kim, H.; Kim, S.-W.; Kang, K. Aqueous Rechargeable Li and Na Ion Batteries. *Chem. Rev.* **2014**, *114* (23), 11788–11827.
- (9) Wang, Y.; Yi, J.; Xia, Y. Recent Progress in Aqueous Lithium-Ion Batteries. *Adv. Energy Mater.* **2012**, *2* (7), 830–840.
- (10) Suo, L.; Borodin, O.; Gao, T.; Olguin, M.; Ho, J.; Fan, X.; Luo, C.; Wang, C.; Xu, K. Water-in-salt[®] electrolyte enables high-voltage aqueous lithium-ion chemistries. *Science* **2015**, *350* (6263), 938–943.
- (11) Suo, L.; Borodin, O.; Sun, W.; Fan, X.; Yang, C.; Wang, F.; Gao, T.; Ma, Z.; Schroeder, M.; von Cresce, A.; Russell, S. M.; Armand, M.; Angell, A.; Xu, K.; Wang, C. Advanced High-Voltage Aqueous Lithium-Ion Battery Enabled by “Water-in-Bisalt” Electrolyte. *Angew. Chem., Int. Ed.* **2016**, *55* (25), 7136–7141.
- (12) Wang, Y.; Meng, X.; Sun, J.; Liu, Y.; Hou, L., Recent Progress in “Water-in-Salt” Electrolytes Toward Non-lithium Based Rechargeable Batteries. *Frontiers in Chemistry* **2020**, *8*, DOI: [10.3389/fchem.2020.00595](https://doi.org/10.3389/fchem.2020.00595).
- (13) Suo, L.; Borodin, O.; Wang, Y.; Rong, X.; Sun, W.; Fan, X.; Xu, S.; Schroeder, M. A.; Cresce, A. V.; Wang, F.; Yang, C.; Hu, Y.-S.; Xu, K.; Wang, C. Water-in-Salt[®] Electrolyte Makes Aqueous Sodium-Ion Battery Safe, Green, and Long-Lasting. *Adv. Energy Mater.* **2017**, *7* (21), 1701189.
- (14) Fichtner, M. Recent Research and Progress in Batteries for Electric Vehicles. *Batteries & Supercaps* **2022**, *5* (2), e202100224.
- (15) Abraham, K. M. How Comparable Are Sodium-Ion Batteries to Lithium-Ion Counterparts? *ACS Energy Letters* **2020**, *5* (11), 3544–3547.
- (16) Didar, B. R.; Groß, A. Solvation structure and dynamics of Li and LiO₂ and their transformation in non-aqueous organic electrolyte solvents from first-principles simulations. *Chinese Journal of Catalysis* **2022**, *43* (11), 2850–2857.
- (17) Borodin, O.; Suo, L.; Olguin, M.; Cresce, A. v.; Vatamanu, J.; Wang, F.; Ren, X.; Dura, J. A.; Faraone, A.; Gobet, M.; Munoz, S.; Greenbaum, S.; Wang, C.; Xu, K. Structure and Transport of “Water-in-Salt” Electrolytes from Molecular Dynamics Simulations. *ECS Meeting Abstracts* **2017**, MA2017-02 (46), 2014.
- (18) Zhang, Y.; Lewis, N. H. C.; Mars, J.; Wan, G.; Weadock, N. J.; Takacs, C. J.; Lukatskaya, M. R.; Steinrück, H.-G.; Toney, M. F.; Tokmakoff, A.; Maginn, E. J. Water-in-Salt LiTFSI Aqueous Electrolytes. 1. Liquid Structure from Combined Molecular Dynamics Simulation and Experimental Studies. *J. Phys. Chem. B* **2021**, *125* (17), 4501–4513.
- (19) Zhang, Y.; Maginn, E. J. Water-In-Salt LiTFSI Aqueous Electrolytes (2): Transport Properties and Li⁺ Dynamics Based on Molecular Dynamics Simulations. *J. Phys. Chem. B* **2021**, *125* (48), 13246–13254.

- (20) Mendez-Morales, T.; Li, Z.; Salanne, M. Computational Screening of the Physical Properties of Water-in-Salt Electrolytes**. *Batteries & Supercaps* **2021**, *4* (4), 646–652.
- (21) Lim, J.; Park, K.; Lee, H.; Kim, J.; Kwak, K.; Cho, M. Nanometric Water Channels in Water-in-Salt Lithium Ion Battery Electrolyte. *J. Am. Chem. Soc.* **2018**, *140* (46), 15661–15667.
- (22) Triolo, A.; Di Liso, V.; Lo Celso, F.; Appetecchi, G. B.; Fazio, B.; Chater, P.; Martinelli, A.; Sciubba, F.; Russina, O. Liquid Structure of a Water-in-Salt Electrolyte with a Remarkably Asymmetric Anion. *J. Phys. Chem. B* **2021**, *125* (45), 12500–12517.
- (23) Gupta, S.; Sappidi, P. Understanding the Molecular-Level Structure and Dynamics of Sodium Ions in Water in Ionic Liquid Electrolytes by Molecular Dynamics Simulations. *J. Chem. Eng. Data* **2023**, *68*, 162.
- (24) Sakti, A. W.; Wahyudi, S. T.; Ahmad, F.; Darmawan, N.; Hardhienata, H.; Alatas, H. Effects of Salt Concentration on the Water and Ion Self-Diffusion Coefficients of a Model Aqueous Sodium-Ion Battery Electrolyte. *J. Phys. Chem. B* **2022**, *126* (11), 2256–2264.
- (25) Da Silva, D. A. C.; Pinzón, M. J. C.; Messias, A.; Fileti, E. E.; Pascon, A.; Franco, D. V.; Da Silva, L. M.; Zanin, H. G. Effect of conductivity, viscosity, and density of water-in-salt electrolytes on the electrochemical behavior of supercapacitors: molecular dynamics simulations and in situ characterization studies. *Materials Advances* **2022**, *3* (1), 611–623.
- (26) Tirado-Rives, J. W. M. D.; Jorgensen, W. L.; Maxwell, D. S.; Tirado-Rives, J. Development and testing of the OPLS all-atom force field on conformational energetics and properties of organic liquids. *J. Am. Chem. Soc.* **1996**, *118* (45), 11225–11236.
- (27) Wang, J.; Wolf, R. M.; Caldwell, J. W.; Kollman, P. A.; Case, D. A. Development and testing of a general amber force field. *J. Comput. Chem.* **2004**, *25* (9), 1157–1174.
- (28) Kartha, T. R.; Mallik, B. S. Ionic conductance and viscous drag in water-in-salt electrolytes for lithium and sodium ion batteries and supercapacitors. *Materials Today Communications* **2020**, *25*, 101588.
- (29) Molinari, N.; Mailoa, J. P.; Kozinsky, B. General Trend of a Negative Li Effective Charge in Ionic Liquid Electrolytes. *Journal of physical chemistry letters* **2019**, *10* (10), 2313–2319.
- (30) Beichel, W.; Trapp, N.; Hauf, C.; Kohler, O.; Eickerling, G.; Scherer, W.; Krossing, I. Charge-Scaling Effect in Ionic Liquids from the Charge-Density Analysis of N,N'-Dimethylimidazolium Methylsulfate. *Angew. Chem., Int. Ed.* **2014**, *53* (12), 3143–3146.
- (31) Cui, K.; Yethiraj, A.; Schmidt, J. R. Influence of Charge Scaling on the Solvation Properties of Ionic Liquid Solutions. *J. Phys. Chem. B* **2019**, *123* (43), 9222–9229.
- (32) Barbosa, G. D.; Liu, X.; O'Harra, K. E.; Bara, J. E.; Turner, C. H. Charge scaling parameter evaluation for multivalent ionic liquids with fixed point charge force fields. *Journal of Ionic Liquids* **2022**, *2* (1), 100020.
- (33) Sun, Z.; Gong, Z.; Zheng, L.; Kalthor, P.; Huai, Z.; Liu, Z. Molecular modelling of ionic liquids: General guidelines on fixed-charge force fields for balanced descriptions. *Journal of Ionic Liquids* **2022**, *2* (2), 100043.
- (34) Jiang, L.; Liu, L.; Yue, J.; Zhang, Q.; Zhou, A.; Borodin, O.; Suo, L.; Li, H.; Chen, L.; Xu, K.; Hu, Y.-S. High-Voltage Aqueous Na-Ion Battery Enabled by Inert-Cation-Assisted Water-in-Salt Electrolyte. *Adv. Mater.* **2020**, *32* (2), 1904427.
- (35) Borodin, O. Polarizable Force Field Development and Molecular Dynamics Simulations of Ionic Liquids. *J. Phys. Chem. B* **2009**, *113* (33), 11463–11478.
- (36) Goloviznina, K.; Gong, Z.; Padua, A. A. H. The CL&Pol polarizable force field for the simulation of ionic liquids and eutectic solvents. *WIREs Computational Molecular Science* **2022**, *12* (3), e1572.
- (37) Drude, P. *The Theory of Optics*; Longmans, Green and Co., 1922.
- (38) Schröder, C.; Steinhauser, O. Simulating polarizable molecular ionic liquids with Drude oscillators. *J. Chem. Phys.* **2010**, *133* (15), 154511.
- (39) Bedrov, D.; Piquemal, J.-P.; Borodin, O.; MacKerell, A. D., Jr.; Roux, B.; Schröder, C. Molecular Dynamics Simulations of Ionic Liquids and Electrolytes Using Polarizable Force Fields. *Chem. Rev.* **2019**, *119* (13), 7940–7995.
- (40) McDaniel, J. G.; Schmidt, J. R. Physically-Motivated Force Fields from Symmetry-Adapted Perturbation Theory. *J. Phys. Chem. A* **2013**, *117* (10), 2053–2066.
- (41) Son, C. Y.; McDaniel, J. G.; Schmidt, J. R.; Cui, Q.; Yethiraj, A. First-Principles United Atom Force Field for the Ionic Liquid BMIM +BF₄⁻: An Alternative to Charge Scaling. *J. Phys. Chem. B* **2016**, *120* (14), 3560–3568.
- (42) McDaniel, J. G.; Son, C. Y. Ion Correlation and Collective Dynamics in BMIM/BF₄-Based Organic Electrolytes: From Dilute Solutions to the Ionic Liquid Limit. *J. Phys. Chem. B* **2018**, *122* (28), 7154–7169.
- (43) McDaniel, J. G. Polarization Effects in Binary [BMIM +][BF₄⁻]/1,2-Dichloroethane, Acetone, Acetonitrile, and Water Electrolytes. *J. Phys. Chem. B* **2018**, *122* (15), 4345–4355.
- (44) Lamoureux, G.; Harder, E.; Vorobyov, I. V.; Roux, B.; MacKerell, A. D. A polarizable model of water for molecular dynamics simulations of biomolecules. *Chem. Phys. Lett.* **2006**, *418* (1), 245–249.
- (45) Kubisiak, P.; Eilmes, A. Molecular Dynamics Simulations of Ionic Liquid Based Electrolytes for Na-Ion Batteries: Effects of Force Field. *J. Phys. Chem. B* **2017**, *121* (42), 9957–9968.
- (46) Leontyev, I.; Stuchebrukhov, A. Accounting for electronic polarization in non-polarizable force fields. *Phys. Chem. Chem. Phys.* **2011**, *13* (7), 2613–2626.
- (47) Duboué-Dijon, E.; Javanainen, M.; Delcroix, P.; Jungwirth, P.; Martinez-Seara, H. A practical guide to biologically relevant molecular simulations with charge scaling for electronic polarization. *J. Chem. Phys.* **2020**, *153* (5), No. 050901.
- (48) Lemkul, J. A.; Huang, J.; Roux, B.; MacKerell, A. D., Jr. An Empirical Polarizable Force Field Based on the Classical Drude Oscillator Model: Development History and Recent Applications. *Chem. Rev.* **2016**, *116* (9), 4983–5013.
- (49) Waibel, C.; Gross, J. Polarizable Transferable Anisotropic United-Atom Force Field Based on the Mie Potential for Phase Equilibria: Ethers, n-Alkanes, and Nitrogen. *J. Chem. Theory Comput.* **2019**, *15* (4), 2561–2573.
- (50) Geerke, D. P.; van Gunsteren, W. F. On the Calculation of Atomic Forces in Classical Simulation Using the Charge-on-Spring Method To Explicitly Treat Electronic Polarization. *J. Chem. Theory Comput.* **2007**, *3* (6), 2128–2137.
- (51) van Maaren, P. J.; van der Spoel, D. Molecular Dynamics Simulations of Water with Novel Shell-Model Potentials. *J. Phys. Chem. B* **2001**, *105* (13), 2618–2626.
- (52) Ferenczy, G. G.; Reynolds, C. A. Modeling Polarization through Induced Atomic Charges. *J. Phys. Chem. A* **2001**, *105* (51), 11470–11479.
- (53) Rupakheti, C. R.; MacKerell, A. D., Jr.; Roux, B. Global Optimization of the Lennard-Jones Parameters for the Drude Polarizable Force Field. *J. Chem. Theory Comput.* **2021**, *17* (11), 7085–7095.
- (54) Harder, E.; Anisimov, V. M.; Vorobyov, I. V.; Lopes, P. E. M.; Noskov, S. Y.; MacKerell, A. D.; Roux, B. Atomic Level Anisotropy in the Electrostatic Modeling of Lone Pairs for a Polarizable Force Field Based on the Classical Drude Oscillator. *J. Chem. Theory Comput.* **2006**, *2* (6), 1587–1597.
- (55) Goloviznina, K.; Canongia Lopes, J. N.; Costa Gomes, M.; Pádúa, A. A. H. Transferable, Polarizable Force Field for Ionic Liquids. *J. Chem. Theory Comput.* **2019**, *15* (11), 5858–5871.
- (56) Groß, A.; Sakong, S. Ab Initio Simulations of Water/Metal Interfaces. *Chem. Rev.* **2022**, *122* (12), 10746–10776.
- (57) Clough, S. A.; Beers, Y.; Klein, G. P.; Rothman, L. S. Dipole moment of water from Stark measurements of H₂O, HDO, and D₂O. *J. Chem. Phys.* **1973**, *59* (5), 2254–2259.
- (58) Taylor, T.; Schmollgruber, M.; Schröder, C.; Steinhauser, O. The effect of Thole functions on the simulation of ionic liquids with

- point induced dipoles at various densities. *J. Chem. Phys.* **2013**, *138* (20), 204119.
- (59) Thole, B. T. Molecular polarizabilities calculated with a modified dipole interaction. *Chem. Phys.* **1981**, *59* (3), 341–350.
- (60) Tang, K. T.; Toennies, J. P. An improved simple model for the van der Waals potential based on universal damping functions for the dispersion coefficients. *J. Chem. Phys.* **1984**, *80* (8), 3726–3741.
- (61) Goloviznina, K.; Gong, Z.; Costa Gomes, M. F.; Pádua, A. A. H. Extension of the CL&Pol Polarizable Force Field to Electrolytes, Protic Ionic Liquids, and Deep Eutectic Solvents. *J. Chem. Theory Comput.* **2021**, *17* (3), 1606–1617.
- (62) Whitfield, T. W.; Varma, S.; Harder, E.; Lamoureux, G.; Rempe, S. B.; Roux, B. Theoretical Study of Aqueous Solvation of K⁺ Comparing ab Initio, Polarizable, and Fixed-Charge Models. *J. Chem. Theory Comput.* **2007**, *3* (6), 2068–2082.
- (63) Rowley, C. N.; Roux, B. t. The Solvation Structure of Na⁺ and K⁺ in Liquid Water Determined from High Level ab Initio Molecular Dynamics Simulations. *J. Chem. Theory Comput.* **2012**, *8* (10), 3526–3535.
- (64) Oostenbrink, C.; Villa, A.; Mark, A. E.; Van Gunsteren, W. F. A biomolecular force field based on the free enthalpy of hydration and solvation: The GROMOS force-field parameter sets 53A5 and 53A6. *J. Comput. Chem.* **2004**, *25* (13), 1656–1676.
- (65) Canongia Lopes, J. N.; Pádua, A. A. H. Molecular Force Field for Ionic Liquids Composed of Triflate or Bistriflylimide Anions. *J. Phys. Chem. B* **2004**, *108* (43), 16893–16898.
- (66) Heid, E.; Szabadi, A.; Schröder, C. Quantum mechanical determination of atomic polarizabilities of ionic liquids. *Phys. Chem. Chem. Phys.* **2018**, *20* (16), 10992–10996.
- (67) Lamoureux, G.; Roux, B. t. Modeling induced polarization with classical Drude oscillators: Theory and molecular dynamics simulation algorithm. *J. Chem. Phys.* **2003**, *119* (6), 3025–3039.
- (68) Heid, E.; Boresch, S.; Schröder, C. Polarizable molecular dynamics simulations of ionic liquids: Influence of temperature control. *J. Chem. Phys.* **2020**, *152* (9), No. 094105.
- (69) Mahan, G. D. Modified Sternheimer equation for polarizability. *Phys. Rev. A* **1980**, *22* (5), 1780–1785.
- (70) Yu, H.; Whitfield, T. W.; Harder, E.; Lamoureux, G.; Vorobyov, I.; Anisimov, V. M.; MacKerell, A. D., Jr.; Roux, B. Simulating Monovalent and Divalent Ions in Aqueous Solution Using a Drude Polarizable Force Field. *J. Chem. Theory Comput.* **2010**, *6* (3), 774–786.
- (71) Li, H.; Ngo, V.; Da Silva, M. C.; Salahub, D. R.; Callahan, K.; Roux, B.; Noskov, S. Y. Representation of Ion–Protein Interactions Using the Drude Polarizable Force-Field. *J. Phys. Chem. B* **2015**, *119* (29), 9401–9416.
- (72) Jiménez-Ángeles, F.; Harmon, K. J.; Nguyen, T. D.; Fenter, P.; Olvera de la Cruz, M. Nonreciprocal interactions induced by water in confinement. *Physical Review Research* **2020**, *2* (4), No. 043244.
- (73) Dočkal, J.; Lísal, M.; Moučka, F. Molecular Force Field Development for Aqueous Electrolytes: 2. Polarizable Models Incorporating Crystalline Chemical Potential and Their Accurate Simulations of Halite, Hydrohalite, Aqueous Solutions of NaCl, and Solubility. *J. Chem. Theory Comput.* **2020**, *16* (6), 3677–3688.
- (74) Noskov, S. Y.; Lamoureux, G.; Roux, B. Molecular Dynamics Study of Hydration in Ethanol–Water Mixtures Using a Polarizable Force Field. *J. Phys. Chem. B* **2005**, *109* (14), 6705–6713.
- (75) Khalid, S.; Pianta, N.; Mustarelli, P.; Ruffo, R. Use of Water-In-Salt Concentrated Liquid Electrolytes in Electrochemical Energy Storage: State of the Art and Perspectives. *Batteries* **2023**, *9* (1), 47.
- (76) Polak, E.; Ribiere, G. Note sur la convergence de méthodes de directions conjuguées. *R.I.R.O.* **1969**, *3* (16), 35–43.
- (77) Dequidt, A.; Devémy, J.; Pádua, A. A. H. Thermalized Drude Oscillators with the LAMMPS Molecular Dynamics Simulator. *J. Chem. Inf. Model.* **2016**, *56* (1), 260–268.
- (78) Hockney, R. W.; Eastwood, J. W. *Computer Simulation Using Particles*; Adam Hilger, 1988.
- (79) Plimpton, S. Fast Parallel Algorithms for Short-Range Molecular Dynamics. *J. Comput. Phys.* **1995**, *117* (1), 1–19.
- (80) Martyna, G. J.; Klein, M. L.; Tuckerman, M. Nosé–Hoover chains: The canonical ensemble via continuous dynamics. *J. Chem. Phys.* **1992**, *97* (4), 2635–2643.
- (81) Kamberaj, H.; Low, R. J.; Neal, M. P. Time reversible and symplectic integrators for molecular dynamics simulations of rigid molecules. *J. Chem. Phys.* **2005**, *122* (22), 224114.
- (82) Tsimpanogiannis, I. N.; Moulτος, O. A.; Franco, L. F. M.; Spera, M. B. d. M.; Erdős, M.; Economou, I. G. Self-diffusion coefficient of bulk and confined water: a critical review of classical molecular simulation studies. *Mol. Simul.* **2019**, *45* (4–5), 425–453.
- (83) Malenkov, G. Structure and dynamics of liquid water. *J. Struct. Chem.* **2006**, *47*, S1–S31.
- (84) Lee, S. H.; Rasaiah, J. C. Molecular Dynamics Simulation of Ionic Mobility. I: Alkali Metal Cations in Water AT 25 C. *J. Chem. Phys.* **1994**, *101*, 6964–6974.
- (85) Zheng, Y.; Zaoui, A. How water and counterions diffuse into the hydrated montmorillonite. *Solid State Ionics* **2011**, *203*, 80–85.
- (86) Stokes, R. The diffusion coefficients of eight uni-univalent electrolytes in aqueous solution at 25. *J. Am. Chem. Soc.* **1950**, *72* (5), 2243–2247.
- (87) Bernard, O.; Cartailier, T.; Turq, P.; Bium, L. Mutual diffusion coefficients in electrolyte solutions. *J. Mol. Liq.* **1997**, *73–74*, 403–411.
- (88) Schröder, C. Comparing reduced partial charge models with polarizable simulations of ionic liquids. *Phys. Chem. Chem. Phys.* **2012**, *14* (9), 3089–3102.
- (89) Bankura, A.; Carnevale, V.; Klein, M. L. Hydration structure of Na⁺ and K⁺ from ab initio molecular dynamics based on modern density functional theory. *Mol. Phys.* **2014**, *112* (9–10), 1448–1456.
- (90) Seo, D. M.; Borodin, O.; Balogh, D.; O’Connell, M.; Ly, Q.; Han, S.-D.; Passerini, S.; Henderson, W. A. Electrolyte Solvation and Ionic Association III. Acetonitrile–Lithium Salt Mixtures—Transport Properties. *J. Electrochem. Soc.* **2013**, *160* (8), A1061.
- (91) Harvey, S. C.; Tan, R. K. Z.; Cheatham, T. E. The flying ice cube: Velocity rescaling in molecular dynamics leads to violation of energy equipartition. *J. Comput. Chem.* **1998**, *19* (7), 726–740.
- (92) Chiu, S.-W.; Clark, M.; Subramaniam, S.; Jakobsson, E. Collective motion artifacts arising in long-duration molecular dynamics simulations. *J. Comput. Chem.* **2000**, *21* (2), 121–131.
- (93) Braun, E.; Moosavi, S. M.; Smit, B. Anomalous Effects of Velocity Rescaling Algorithms: The Flying Ice Cube Effect Revisited. *J. Chem. Theory Comput.* **2018**, *14* (10), 5262–5272.
- (94) Landesfeind, J.; Hosaka, T.; Graf, M.; Kubota, K.; Komaba, S.; Gasteiger, H. A. Comparison of Ionic Transport Properties of Non-Aqueous Lithium and Sodium Hexafluorophosphate Electrolytes. *J. Electrochem. Soc.* **2021**, *168* (4), No. 040538.
- (95) Morales, D.; Chagas, L. G.; Paterno, D.; Greenbaum, S.; Passerini, S.; Suarez, S. Transport studies of NaPF₆ carbonate solvents-based sodium ion electrolytes. *Electrochim. Acta* **2021**, *377*, 138062.
- (96) Pham, T. A.; Kweon, K. E.; Samanta, A.; Lordi, V.; Pask, J. E. Solvation and Dynamics of Sodium and Potassium in Ethylene Carbonate from ab Initio Molecular Dynamics Simulations. *J. Phys. Chem. C* **2017**, *121* (40), 21913–21920.
- (97) Hayamizu, K.; Aihara, Y.; Arai, S.; Martinez, C. G. Pulse-Gradient Spin-Echo ¹H, ⁷Li, and ¹⁹F NMR Diffusion and Ionic Conductivity Measurements of 14 Organic Electrolytes Containing LiN(SO₂CF₃)₂. *J. Phys. Chem. B* **1999**, *103* (3), 519–524.
- (98) Capiglia, C.; Saito, Y.; Kageyama, H.; Mustarelli, P.; Iwamoto, T.; Tabuchi, T.; Tukamoto, H. ⁷Li and ¹⁹F diffusion coefficients and thermal properties of non-aqueous electrolyte solutions for rechargeable lithium batteries. *J. Power Sources* **1999**, *81–82*, 859–862.
- (99) Hayamizu, K. Temperature Dependence of Self-Diffusion Coefficients of Ions and Solvents in Ethylene Carbonate, Propylene Carbonate, and Diethyl Carbonate Single Solutions and Ethylene Carbonate + Diethyl Carbonate Binary Solutions of LiPF₆ Studied by NMR. *Journal of Chemical & Engineering Data* **2012**, *57* (7), 2012–2017.

(100) Ong, M. T.; Verners, O.; Draeger, E. W.; van Duin, A. C. T.; Lordi, V.; Pask, J. E. Lithium Ion Solvation and Diffusion in Bulk Organic Electrolytes from First-Principles and Classical Reactive Molecular Dynamics. *J. Phys. Chem. B* **2015**, *119* (4), 1535–1545.

(101) Karatrantos, A.; Ohba, T.; Cai, Q. Diffusion of ions and solvent in propylene carbonate solutions for lithium-ion battery applications. *J. Mol. Liq.* **2020**, *320*, 114351.

(102) Neuhaus, J.; Bellaire, D.; Kohns, M.; von Harbou, E.; Hasse, H. Self-Diffusion Coefficients in Solutions of Lithium Bis-(fluorosulfonyl)imide with Dimethyl Carbonate and Ethylene Carbonate. *Chemie Ingenieur Technik* **2019**, *91* (11), 1633–1639.

(103) Borodin, O.; Smith, G. D. LiTFSI Structure and Transport in Ethylene Carbonate from Molecular Dynamics Simulations. *J. Phys. Chem. B* **2006**, *110* (10), 4971–4977.

(104) Wróbel, P.; Kubisiak, P.; Eilmes, A. MeTFSI (Me = Li, Na) Solvation in Ethylene Carbonate and Fluorinated Ethylene Carbonate: A Molecular Dynamics Study. *J. Phys. Chem. B* **2021**, *125* (4), 1248–1258.